In Silico Model for Determination of In Vivo Pre-Stretch in Neonatal and Adult Murine Cranial Dura Mater

Jack Consolini

Publication Date

23-11-2022

IN SILICO MODEL FOR DETERMINATION OF *IN VIVO* PRE-STRETCH IN NEONATAL AND ADULT MURINE CRANIAL DURA MATER

A Thesis

Submitted to the Graduate School
of the University of Notre Dame
in Partial Fulfillment of the Requirements
for the Degree of

Master of Science
in
Mechanical Engineering

by

Jack Consolini

Maria Holland, Director

Graduate Program in Aerospace and Mechanical Engineering
Notre Dame, Indiana
December 2022

IN SILICO MODEL FOR DETERMINATION OF *IN VIVO* PRE-STRETCH IN NEONATAL AND ADULT MURINE CRANIAL DURA MATER

Abstract

by

Jack Consolini

Cranial dura mater is a dense interwoven vascular connective tissue that protects the brain and helps regulate neurocranial remodeling during head development. *In vivo* investigations indicate that the tissue mediates cranial suture fusion by responding to strains from the growing brain. *Ex vivo* experimentation has attempted to characterize the mechanical properties that make the dura an effective mechanoreceptor and mechanotransmitter; however, they fail to capture key characteristics of the dura *in vivo*, such as the impact of tissue pre-stretch. Residual strain, or pre-stretch, is an important quality of many biological tissues, and when not accurately captured by *ex vivo* experiments, generally leads to underestimation of mechanical stiffness. Considering the importance and lacking characterization of dural pre-stretch, this study aimed to create a robust *in silico* model for determination of *in vivo* pre-stretch in neonatal and adult murine cranial dura mater. Transverse and longitudinal incisions were performed *ex vivo* in the parietal dura of newborn (day $\sim$4) and mature (day 60+) mice. *In silico* models of incised neonatal and adult dura experiencing isotropic stretching in the plane transverse to the model's surface normal were simulated in Abaqus/Standard. The *ex vivo* and *in silico* incision opening ratios (opening width over length) were compared, allowing the *in vivo* in-plane pre-stretch to be determined. Images of cut openings and estimations of pre-stretch

indicate the dural pre-stretch is direction-dependent. Differences in neonatal and adult pre-stretch provided further insight into the age-dependency of murine cranial dura mater pre-stretch.

CONTENTS

FIGURES

TABLES

ACKNOWLEDGEMENTS

I would like thank my advisor, Dr. Maria Holland, for supporting my master studies and guiding me to becoming a more capable engineer and researcher. Working under such an intelligent and enthusiastic scientist has exponentially improved my understanding of mechanical engineering science, allowing me to engage with the complex problems characteristic to the biomechanical field.

I am very grateful for my time at Notre Dame and the professors that have broadened my knowledge of applied mathematics, solid mechanics, and human biology and kinematics. I offer a special thank you to Dr. Craig Goehler for being an exemplary academic role model. Finally, thank you Dr. Parisa Saboori and Dr. Graham Walker of Manhattan College for the tools and confidence to continue my academic career.

I would like to thank my parents, family, and friends for continued emotional support throughout my master studies. I was fortunate to have grown up in a household with a mother and father who loved each other, and my sister and I, deeply. They instilled the importance of having compassion and the desire to help others; the foremost values that guide my research pursuits. Thank you Michaela for being an exemplary older sister and friend. Special thanks to: Lauren, Patrick, Fatemeh, and David here at Notre Dame; Cate, Tomo, John, Adam, Rory, Chris, and Amir from Manhattan College; and Jack, Kenny, Felix, Army, Bobby, Matt, Chris, Mike, Santosh, David, and John back in Darien. I am consistently in awe of how I have been surrounded by unwaveringly good and caring friends. I hope to always be there for you all, as much as you have been there for me.

CHAPTER 1

INTRODUCTION

1.1 Motivation

Scientific and clinical research of mammalian brain and skull development provide evidence that the cranium expands concurrently with the growing brain. Computational [1–3] and experimental [4–6] studies looking to better understand cranial maturation have implicated the meninges—tissues that surround and protect the brain and spinal cord—as very important mechanoreceptors and mechanotransmitters. In particular, the dura mater, the outermost meningeal layer fixed to the calvaria, is responsible for properly timing and pacing the ossification of the cranial sutures [7–11]. Pressure from the growing brain fosters morphological remodeling of the cranial vault [6], separating the diploic bone plates [12] and avoiding increased pressure on the cerebral cortex. Neurocranial expansion induces quasi-static tensile strains within the cranial sutures, leading to mineralization of the fibrous joints via endochondral ossification [6]. The dura mater controls suture fusion by timely provision of extracellular matrix molecules and release of osteogenic growth factors and cytokines [6]. In pathological growth cases, such as those of craniofacial malformations (including craniosynostoses), the dura mater improperly senses pressure from the brain, leading the cranial sutures to prematurely fuse [6, 13, 14]. Healthy suture fusion is dependent on the cranial dura having the correct physical and mechanical properties, allowing it to appropriately respond to mechanical loads.

The dura mater's thickness, stiffness, elasticity, permeability, hardness, and strength affect how the tissue experiences strain. A significant body of work [13, 15–27] has

studied the mechanical properties of mammalian (human, porcine, and rodent) dura mater, offering some characterization of the tissue's material behavior. At this point, it is understood that mammalian dura mater deforms non-linearly [13, 16, 19, 20, 22, 23, 27] and in a time-dependent manner [20, 22, 28, 29], acting as a hyperelastic and viscoelastic material. Additionally, cranial dura appears to have globally uniform physical and mechanical properties [19, 26], with local variation due to changes in thickness [30–32] and collagen alignment/structure [5, 21, 25, 26]. The major limitation of these works is that the dura mater was tested in an environment foreign to its *in vivo* conditions. Many investigations performed uniaxial [15, 20, 23, 24, 26, 27] or biaxial [16, 19, 23] tensile tests on freshly excised or preserved samples with simple geometries (typically dumbbell, rectangle, or square). The *ex vivo* experiments fail to capture important characteristics of the dura mater's *in situ* environment, such as the impact of the tissues curvature or firm connection to the skull. Moreover, aside from generic pre-conditioning done prior to loading, almost all studies neglect to consider the residual strain or pre-stretch the dura mater experiences *in vivo*.

Like many biological tissues, the dura mater naturally exists in a "pre-stretched" state, where the material is constantly under tension or pressure due to interactions with other soft tissues and surrounding bones. Significant research has shown that ignoring the pre-stretch of a tissue can drastically alter the calculation of the material's mechanical properties [33–36]. Non-linearly elastic materials, like dura mater, generally have different stiffness regimes at varying strains, thus, disregarding pre-stretch may mean the tissue is actually deforming below or outside of its apposite operating range [35]. Most *ex vivo* investigations overlook pre-stretch, generally leading the mechanical stiffness to be underestimated. This can have significant clinical implications, especially for patients with cranial facial malformations.

For example, newborns suffering with craniosynostoses can receive early surgical interventions—such as cranioplasty [37] and spring-assisted cranioplasty (SAC)

[38]—to alleviate increased intracranial pressure. Safety and efficacy of the procedures strongly rely on the dura remaining intact, for tearing could lead to vascular leakage or infection [37]. In the case of SAC, the implanted spring must have the right stiffness so that the dura is not stretched beyond its *in vivo* ultimate tensile strength. If the tissue is to tear, autografts and synthetic materials can be used to repair the dura. Yet, additional ailments, such as infectious lesions [39], can arise if the replacement material is not mechanically and biologically compatible. In this example, the distinction between *in vivo* and *ex vivo* stiffness becomes important, as the value affects the tools and success of surgical intervention.

The merit of the current work is predicated on the evident importance of understanding the *in vivo* mechanics of the dura-calvaria boundary. This study of murine cranial dura mater pre-stretch was completed with the intent to offer preliminary steps toward the creation of even more robust, validated models of human dural pre-stretch. Eventually, intricate, patient-specific geometries with experimentally determined parameters may lead to safer and more effective treatments for cranial growth pathologies.

1.2 Background

The dura mater is the thickest and toughest of the meningeal membranes and comprised of two layered sheets: the periosteal (outer) and meningeal (inner) layer [40]. Each layer is composed of collagen fibers; however, the periosteal has a more locally irregular collagen structure than the meningeal, and contains fibroblasts and bone-tissue-producing osteoblasts [21, 25]. The entirety of the dura mater is a vascularized tissue, yet, the outer layer is significantly less vascular than the inner [41]. Examinations of material structure [5, 7, 21, 25] indicate the differences between the meningeal and periosteal tissue reflect the dura's primary functions: 1) supplying blood and nutrients to the head and 2) regulating cranial suture fusion. The highly vascularized inner layer provides adequate blood supply to the skull and other

meningeal tissues, while also jettisoning cellular waste products [41]. Studies of brain and skull growth [8, 21, 42] have shown that osteoblast residence in the outer layer is important, as it contributes bone cells necessary for appropriately timed mineralization of a suture site.

Initially fibrous cranial sutures fuse the gaps between cranial plates via endrochondral bone formation: the soft temporary tissue is replaced with firm cortical bone [6, 43]. Suture mineralization begins once the osteoblasts and their precursors are instructed to migrate from the dura mater and calvaria to the suture surface [11]. The dura encourages osteoblast proliferation by prompting the release of biochemical signals that have been triggered by increased pressure from the developing cortex. The dura acts as a biological strain gauge, thus it is imperative that the tissue properly deforms to applied strains. Alteration of the dura's mechanical properties, via changes in material composition or residual stresses, could inhibit the tissue's ability to cue osteoblastic differentiation, leading to cranial disfigurement. Common pathologies such as premature suture fusion, or craniosyostoses, can be effectively resolved with surgical intervention [37, 38, 44]. However, improved treatment is dependent upon better characterization of the dura mater's *in vivo* mechanical environment, in particular, the tissue's pre-stretch.

While pre-stretch has not been deeply studied in the case of cranial dura mater, the study of residual strains and stresses has been heavily reported on within the broader field of tissue mechanics. The classical procedure for investigating residual strain was instituted by Fung and Liu [45] and Han and Fung [33], who performed cut experiments into arterial tissue. By measuring the opening angle of an incised artery, Fung effectively quantified the residual strain in the direction normal to the cut. Subsequent work and technological improvements have expanded on Fung's methods [35, 46, 47] and tissues of interest, including the gastrointestinal tract [48], skin [49–51], and even the brain [52]. A principal through-line of these works is the

indication of inconsistencies between *ex vivo* and *in vivo* measurements [35].

Firstly, strains measured *ex vivo* are generally larger than *in vivo* estimations [35]. *Ex vivo* tissue is loaded from zero stretch, leading to over-estimation of the available linear toe region. Most tissues are relatively less compliant *in vivo*, and are often residually stressed into their rigid regime. For example, multiple *in vivo* experiments have recorded cardiac valve leaflets are naturally strained between 5% and 10% [53, 54]. Physiologically, the *in vivo* collagen fibrils have already experienced a degree of straightening, while *ex vivo* fibers are wavy and stress-free. Secondly, stress-strain curves obtained from *ex vivo* mechanical testing generally under-estimate *in vivo* stiffness. Many soft tissues, like dura mater, have the ability to withstand incredibly high elastic deformation. *Ex vivo* testing systemically reports lower stiffnesses than *in vivo* estimates [35], likely because deceased tissue has different physical properties. Excised tissues are often softer and weaker because the dehydrated, dead tissue is more brittle. This phenomenon can be observed when looking at fresh versus preserved samples of dura mater; McGarvey et al. [21] reported a reduction in stiffness of the preserved human dura mater (fresh: $61.5 \pm 9.6\,\mathrm{MPa}$, preserved: $45.2 \pm 3.0\,\mathrm{MPa}$).

Advancements in medical imaging technology and minimally invasive analyses have better articulated the effects of *in vivo* pre-stretch on stiffness [55]. Simultaneously, computational methods have been utilized to bridge the gaps between *ex vivo* and *in vivo* investigations. Recent efforts by Henderson et al. [28] and Rausch and Kuhl [35] have demonstrated how effective finite element analyses can be for determination of *in vivo* pre-stretch, and have inspired the current work.

Henderson et al. [28] aimed to determine the magnitude and age-dependency of residual strain in rat cranial dura mater. This was accomplished by preforming transverse and longitudinal incisions on the parietal dura of immature and mature rats (post-natal day 2-26). Henderson et al. [28] created a finite element model of the dural incisions and applied a series of transverse and longitudinal displacements to

the model, thus obtaining an expression which related the *in silico* incision opening widths and lengths to the applied directional strains. They offered estimated values for average residual strain across the different post-partum days, however, the analysis was significantly limited by the simplicity of the computational model. Their model neglected to consider the *in vivo* geometry and non-linear stress-strain behavior of rodent cranial dura mater. To improve upon the previous work, this study aimed to create robust *in silico* models that are more closely reminiscent of the neonatal and adult murine dura's *in vivo* geometry and material behavior. The second objective was to determine the *in vivo* pre-stretch associated to *ex vivo* transverse and longitudinal dural incisions. The final objective was to examine the age-dependency of the *in vivo* in-plane pre-stretch.

The newly developed models approximate the dura mater as a neo-Hookean solid with isotropic material behavior and homogeneous material properties. The material model was calibrated to experimental data of rat cranial dura deformation under uniaxial tension. The tissue was modeled as a three-dimensional 1/8 ellipsoid geometry, which was scaled to both the neonate and adult mice sizes. Taking inspiration from the theory of finite growth in soft tissues [56] and the kinematic description of pre-strain [35], a mathematical model was applied to simulate isotropic stretching in the plane transverse to the *in silico* model's surface normal. The resulting computational incision opening ratios (opening width over length) were compared to experimental values obtained from a concurrent experimental study of *ex vivo* dural incisions performed in newborn (day $\sim$4) and adult (day 60+) mice. Chapter 2 details the *ex vivo* slitting experiment and development of the murine cranial dura pre-stretch model. The determined *in vivo* in-plane pre-stretch is discussed in Chapter 3, along with the experimental and computational limitations of the investigation. Chapter 4 concludes this thesis by summarizing the significant findings and providing insight into potential future directions.

CHAPTER 2

METHODOLOGY

2.1 *Ex vivo* murine dural incision

2.1.1 *Ex vivo* dural incision

Time-dated pregnant adult (day 60+) female Institute of Cancer Research (ICR) mice were purchased from Envigo (Indianapolis, IN). The pregnant females were housed and fed for roughly five days in a temperature- and light-controlled environment. Upon birth of the pups—normally a day after the mice were received—the newborn mice were housed with the adult females until each group were sacrificed, dissected, and incised. The entirety of the sacrifice, dissection, and dural incision of the murine cranial dura mater was carried out by Dr. Alyssa Oberman, within the animal care and use guidelines outlined by the University of Notre Dame.

Four days after birth, the adult mice were sacrificed via euthanasia using a Euthanex chamber to induce CO_2 inhalation. The neonatal mice were sacrificed via euthanasia through decapitation after being anesthetized in a bell jar with isoflourane. After sacrifice, the head was separated from the body and the cranium and dura mater were dissected from the remaining head tissue. Dissection was completed within three hours of sacrifice. The dissection procedure follows: removal of the skin, cutting the skull open along the lower jaw line, removal of the nasal bone, and careful scooping out of the brain. This left the dura mater in tact along the frontal, parietal, and occipital lobes of the cranium. It was important that the dura mater was not scraped off of the interior skull, as the adhesion to the skull maintained the

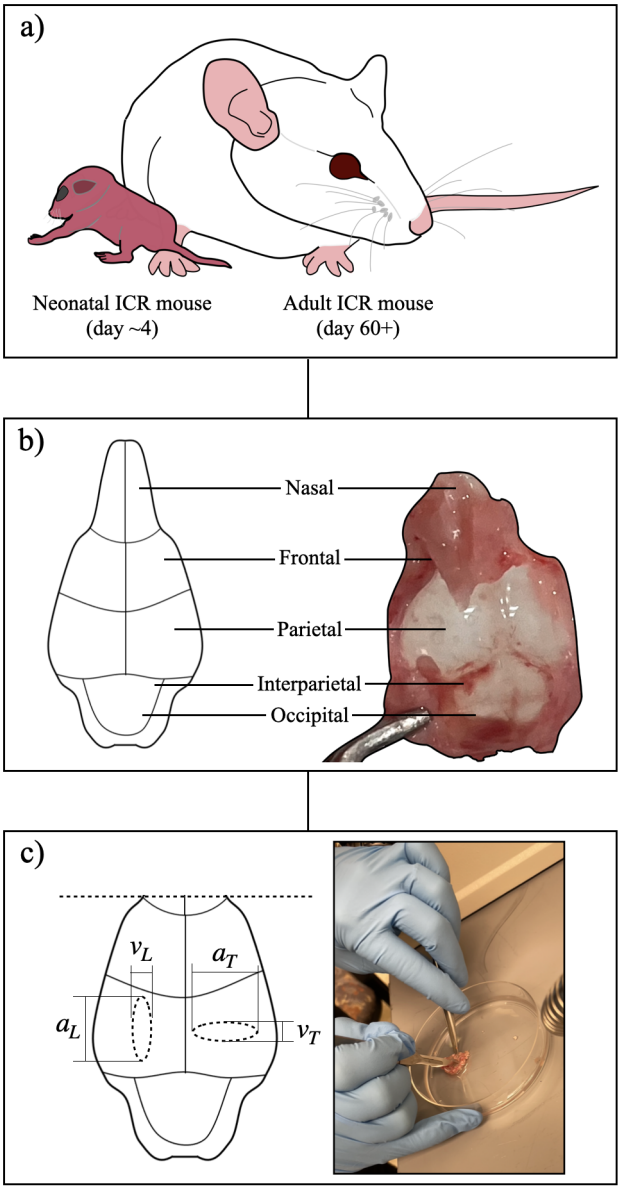

Figure 2.1. Procedure for *ex vivo* dural incision on neonatal and adult murine cranial dura mater. a) Pregnant adult female ICR mice (day 60+) obtained from Envigo (Indianapolis, IN) were housed until giving birth to mice pups. b) On postpartum day four, the two age groups are sacrificed, with their cranium and dura mater dissected within three hours of sacrifice. Care was taken to extract the dura mater intact with the calvaria, to capture the *in situ* conditions. c) Transverse and longitudinal cuts were made with a no. 11 blade scalpel within the parietal lobe. Images were taken immediately after and five minutes later using a Nikon AZ 100 Marco/Zoom Scope with a Nikon DS-L2 camera unit attached to the microscope.

dura's stretched configuration, even once the mouse is deceased. Additional tissue was stripped away to avoid obscuring the cut area along the calvaria.

A no. 11 blade scalpel was used to incise the dissected dura mater while immersed in Phosphate buffer saline. Dr. Oberman made longitudinal (anterior-posterior) and transverse (medial-lateral) incisions from the superior position over the upside-down skull, attempting to make slits along the middle of the medial-lateral distance in the parietal dura. Care was taken to make uniformly sized incisions, however, incisions were manually located within the middle of the extremely small skulls, leading to significant deviations in cut sizes and locations. Images were taken of the incision immediately after cutting and five minutes later, to capture the tissue's relaxation to a new static equilibrium. Images were taken using a Nikon AZ 100 Marco/Zoom Scope with a Nikon DS-L2 camera unit attached to the microscope. Images of the incisions were captured at a variety of magnifications, however, the mature and immature dural cuts were primarily recorded at 3x and 4x scale, respectively. Across three experimental dates, images of 15 dural incisions from 11 subjects (n=5 neonatal, n=6 adult) at two time points were recorded and measured (Table 2.1). When possible, both cut orientations were performed for a single subject. Additional images were taken of the fully dissected cranium without the nasal lobe, allowing the dimensions of the skull to be measured and used for estimation of the *in silico* model's dimensions.

TABLE 2.1

EX VIVO TEST SUBJECTS (n) AND DURAL INCISION SAMPLES BY AGE GROUP

Age-group	n	Transverse	Longitudinal
Neonate	5	2	5
Adult	6	4	4

2.1.2 *Ex vivo* measurement of cranium and dural incision

The post processing of the 15 dural incision images and skull dimensions was conducted using the Java-based image processing program, ImageJ [57]. The images were scaled to their appropriate magnification and all dimensions were measured using the distance tool.

The cranium length, width, and height were used to create the *in silico* ellipsoids, making the models more reminiscent of the *in vivo* tissue curvature and its effects on the incision opening dimensions. The skull dimensions were measured by visually approximating the boundaries of samples in the lateral, anterior, and posterior views of the neonatal (Figure 2.2, left) and adult mice (Figure 2.2, right). While the dura mater was not visible, the crania were so thin that it was assumed there was nearly negligible difference in the skull and dura's length, width, and height.

The thickness of the dura mater—on the order of 0.001mm—could not be measured by from images. Instead, murine dural thickness was estimated from the scaling down of previously measured rodent dural thickness (0.049 ± 0.015mm) from Kinaci

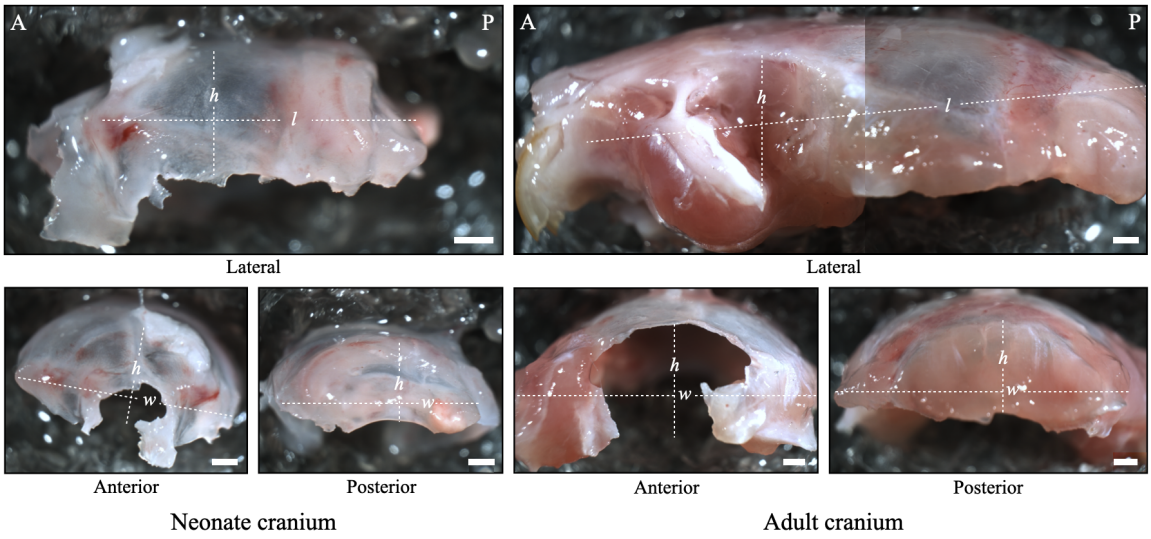

Figure 2.2. Post processing of experimental images using ImageJ. Measurement of neonatal (left) and adult (right) mice skull/dura mater dimensions used for creation of the *in silico* model. All scale bars indicate 1mm.

et al. [58]. Scaling from rat dura was an appropriate approximation for average thickness because rats and mice are anatomically very similar [59, 60]. A simple proportionality relation,

$$\frac{t_{\mathrm{d,M}}}{t_{\mathrm{s,M}}} = \frac{t_{\mathrm{d,R}}}{t_{\mathrm{s,R}}}, \tag{2.1}$$

was used, where the adult mouse dural ($t_{\mathrm{d,M}}$) and skull thickness ($t_{\mathrm{s,M}}$) were related to the adult rat's dural ($t_{\mathrm{d,R}}$) and skull ($t_{\mathrm{s,R}}$) thickness. O'Reilly et al. [61] offered an estimation for mouse and rat skull thickness (0.02mm and 0.71 ± 0.03mm, respectively), enabling the calculation of the estimated adult mouse's dural thickness. The thickness of the neonatal mice dura mater was further scaled down from the estimation for the adult. Again because of the visual measurement limitations, it was difficult to tell just how much the neonatal dura mater decreased in thickness from the adult. Thus, another proportionality relation was used to estimate the newborn

dural thickness ($t_{\mathrm{d,m}}$):

$$\frac{t_{\mathrm{d,m}}}{t_{\mathrm{d,M}}} = \text{average}\left(\frac{l_{\mathrm{s,m}}}{l_{\mathrm{s,M}}}; \frac{w_{\mathrm{s,m}}}{w_{\mathrm{s,M}}}; \frac{h_{\mathrm{s,m}}}{h_{\mathrm{s,M}}}\right), \tag{2.2}$$

using the average of the ratios of adult and neonate dimensions, where m subscripts denote neonatal measurements and M remains associated to the adult mice. While the dura mater in other mammalian species has been shown to globally vary in thickness throughout the calvaria [30, 31], the *in silico* model assumes homogeneous thickness throughout. Heterogeneous thickness was expected to have negligible effects on the *in silico* model's dural incision openings, because the thickness of both age-groups was on the order or less than 0.001mm (Table 2.2).

TABLE 2.2

EX VIVO CRANIUM MEASUREMENTS AND CALCULATED QUANTITIES

Age-group	l (mm)	w (mm)	h (mm)	t (mm)
Neonate	8.674	8.555	2.884	0.00138
Adult	18.630	13.012	4.586	0.00081

The incision opening lengths (a) and widths (v) were recorded for all samples, and the width:length ratio was calculated. For reproducibility, the widths were measured at 0.25, 0.50, and 0.75 of the total incision opening length. The lengths and widths were re-measured three times over the course of three weeks to account for some potential variations that could have arisen from human error. The cut lengths and widths for the 15 dural incisions from 11 subjects (n=5 neonatal, n=6 adult) were

averaged according to cut orientation and age-group (Table 2.3).

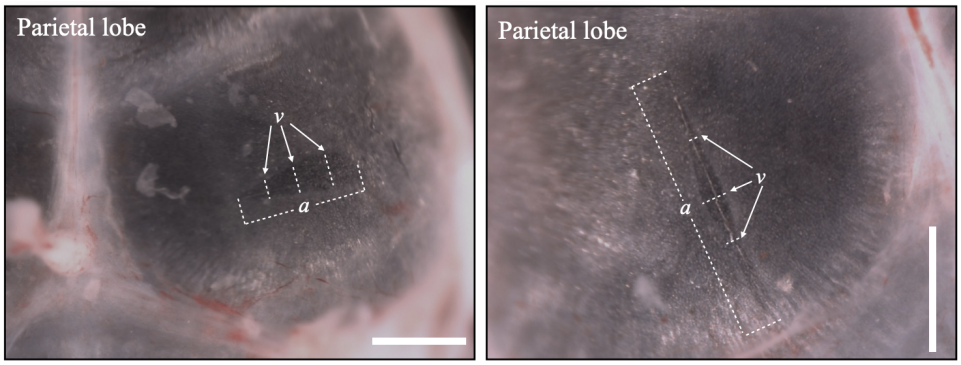

Figure 2.3. Measurement of incision opening lengths (a) and widths (v). Widths were measured at 0.25, 0.50, and 0.75 of the total length. All scale bars indicate 1mm.

TABLE 2.3

EX VIVO DURAL INCISION OPENING WIDTH AND LENGTH MEASUREMENTS

Age-group	Cut orientation	a	$v(0.25a)$	$v(0.50a)$	$v(0.75a)$
Neonate	Transverse	1.06 ± 0.74	0.20 ± 0.08	0.22 ± 0.08	0.19 ± 0.11
Neonate	Longitudinal	1.82 ± 0.44	0.15 ± 0.10	0.19 ± 0.09	0.14 ± 0.08
Adult	Transverse	1.75 ± 0.39	0.35 ± 0.15	0.42 ± 0.15	0.33 ± 0.13
Adult	Longitudinal	2.56 ± 0.30	0.16 ± 0.06	0.23 ± 0.08	0.21 ± 0.07

* Measurements reported in millimeters.

2.2 *In silico* murine dural incision

2.2.1 Kinematic model of pre-stretch

In the current study, the kinematics of pre-stretch are accomplished by modifying certain aspects of the theory of finite growth in elastic soft tissues introduced by Rodriguez et al. [56]. Rodriguez et al. [56] models growth kinematics by decomposing finite growth of an elastic material into first the stress-free addition or removal of material, followed by the elastic deformation of the tissue. This approach insures growth is accomplished without introducing discontinuities. The mathematical model that applies finite stretching is visualized in Figure 2.4 and discussed within this section.

The initial geometry created in Abaqus begins as the stress-free reference body B_{Abaqus}, fixed in space with material points $\boldsymbol{x}_{\text{Abaqus}}$. The motion of the material points as they deform from the referential body to the *in vivo* pre-stretched configuration are described as a function of the material points and time: $\boldsymbol{x}_{\text{p}} = \varphi(\boldsymbol{x}_{\text{Abaqus}}, t)$. In taking the gradient of the mapping function with respect to the material points, the deformation gradient and its Jacobian are given:

$$\boldsymbol{F} = \nabla\varphi, \quad \text{where} \quad J = \det \boldsymbol{F} > 0. \tag{2.3}$$

$\boldsymbol{F}$ and J act as the fundamental measures of fiber and volume changes of a material from one configuration to another, respectively.

The initial body rigidly deforms to the pre-stretched configuration, thus there is no relative motion between $\boldsymbol{x}_{\text{Abaqus}}$ and $\boldsymbol{x}_{\text{p}}$ and no volume change. The issue arises then, if $\boldsymbol{F}$ simply equals the identity matrix ($\boldsymbol{I}$), elastic stretch must be induced by another means. This is accomplished by preforming the multiplicative decomposition of the deformation gradient.

$$\boldsymbol{F} = \boldsymbol{F}^{\text{p}} \cdot \boldsymbol{F}^{0}. \tag{2.4}$$

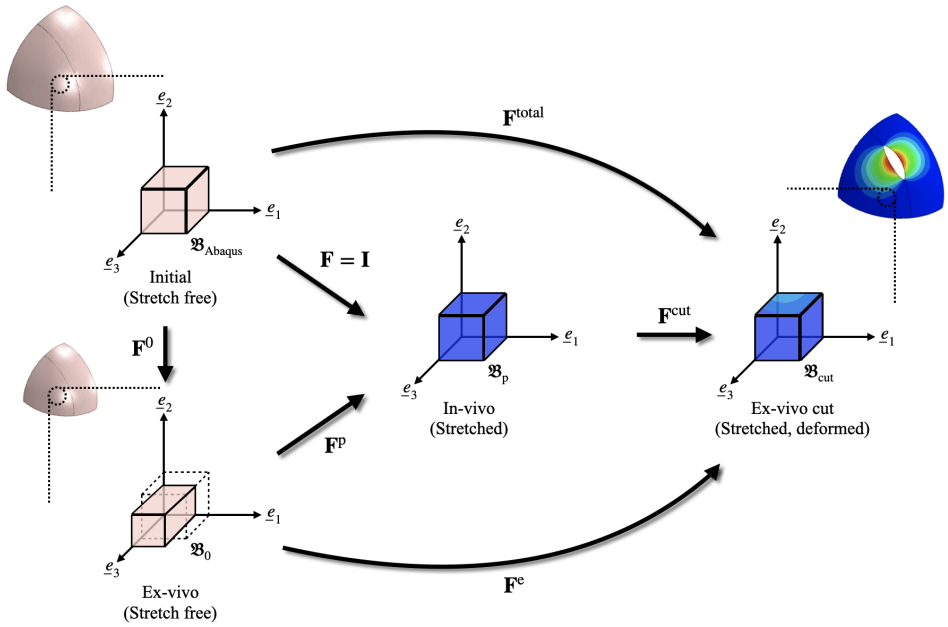

Figure 2.4. Kinematics of finite stretching and post-dural incision deformation of the murine cranial dura mater. The 1/8 ellipsoid shapes are the idealized geometry which represent the neonate and adult dura. The initial stress-free model (top left) is a fictitious configuration only known to Abaqus. The *in vivo* stretched configuration is created through two deformations, one which creates a thicker, smaller tissue ($\boldsymbol{F}^0$) and one which stretches it elastically to achieve the same geometry under pre-stretch ($\boldsymbol{F}^{\text{p}}$). The post-dural incision deformation ($\boldsymbol{F}^{\text{e}}$), resulting in the cut tissue (right), is determined from $\boldsymbol{F}^{\text{e}} = \boldsymbol{F}^{\text{total}} \cdot (\boldsymbol{F}^0)^{-1}$, where $\boldsymbol{F}^{\text{total}}$ is the total deformation recorded by Abaqus.

$\boldsymbol{F}^0$ describes the irreversible re-arrangement of the material, into an intermediate stress-free configuration. This configuration is reminiscent of the *ex vivo* state of the dura mater, in which the excised tissue, free of bony attachments, retracts to a smaller, stiffer sample. From this intermediate configuration, $\boldsymbol{F}^{\text{p}}$ applies an elastic deformation to return the material points to their original location, maintaining compatibility while finitely stretching the solid.

On a similar vein, J can be multiplicatively decomposed,

$$J = J^{\text{p}} J^0, \tag{2.5}$$

where J^0 is the volume change resulting from re-arrangement and J^{p} represents the volume change enforced by elastic deformation. J^{p} characterizes the compressibility behavior by returning the material point's back to their initial configuration.

In assuming the material is nearly incompressible ($J^{\mathrm{p}} \approx 1$), all stretching along the material's principal directions will be dependent on one scalar stretch parameter, λ_{p}. λ_{p} was applied in the two planar directions transverse to the undeformed unit normal vector ($\boldsymbol{n}_0$) at each point along the *in silico* model's outer surface. Rausch and Kuhl [35] offered an expression for the deformation due to transversely isotropic stretching:

$$\boldsymbol{F}^{\mathrm{p}} = \lambda_{\mathrm{p}}[\boldsymbol{I} - \boldsymbol{n}_0 \otimes \boldsymbol{n}_0] + \frac{1}{\lambda_{\mathrm{p}}^2}\boldsymbol{n}_0 \otimes \boldsymbol{n}_0. \tag{2.6}$$

Within Equation 2.6, the first term is associated with the in-plane stretching, while the second term defines the thickness contraction as a product of in-plane stretch. Isotropic stretching was believed to be a fair approximation of the applied pre-stretch because several studies have reported the dura mater behaves isotropically [20, 21, 26, 32, 62].

The stress in the tissue is a function only of the elastic stretch, $\boldsymbol{F}^{\mathrm{e}}$, which can be found directly from $\boldsymbol{F}^{\mathrm{total}}$, a known quantity within Abaqus. Like $\boldsymbol{F}$ and $\boldsymbol{F}^{\mathrm{p}}$, $\boldsymbol{F}^{\mathrm{total}}$ and $\boldsymbol{F}^{\mathrm{e}}$ are related through $\boldsymbol{F}^0$. Using the knowledge that

$$\boldsymbol{F} = \boldsymbol{I}, \text{ thus, } \boldsymbol{F}^{\mathrm{p}} = (\boldsymbol{F}^0)^{-1}, \tag{2.7}$$

the total deformation of the model, can be rewritten in terms of the planar pre-stretch, yielding an expression for the elastic deformation:

$$\boldsymbol{F}^{\mathrm{e}} = \boldsymbol{F}^{\mathrm{total}} \cdot (\boldsymbol{F}^0)^{-1} = \boldsymbol{F}^{total}\left[\lambda_{\mathrm{p}}[\boldsymbol{I} - \boldsymbol{n}_0 \otimes \boldsymbol{n}_0] + \frac{1}{\lambda_{\mathrm{p}}^2}\boldsymbol{n}_0 \otimes \boldsymbol{n}_0\right]^{-1}. \tag{2.8}$$

This method allows in-plane stretch to be easily related to the change in incision

opening dimensions. λ_{p} was set to linearly increase with analysis increment time, (t_i),

$$\lambda_{\mathrm{p},i} = \beta t_i + 1.0, \text{ where, } \beta = \frac{(\lambda_{\mathrm{p},f} - 1.0)}{t_f}, \tag{2.9}$$

and t_f is the total analysis time, and $\lambda_{\mathrm{p},f}$ is the maximum prescribed in-plane stretch.

While properly computing $\boldsymbol{F}^{\mathrm{e}}$ ensures conservation of mass within the closed system, all other forces must be balanced using Cauchy's first equation of motion. The continuum formulation of the balance of linear momentum in the local form,

$$\rho \ddot{\boldsymbol{x}} = \nabla \cdot \boldsymbol{\sigma} + \boldsymbol{B}, \tag{2.10}$$

relates the acceleration of the body, with density ρ, to the body forces, $\boldsymbol{B}$, and divergence of the Cauchy stress, $\nabla \cdot \boldsymbol{\sigma}$ [63]. With no active body forces applied and inertial forces neglected because the model quasi-statically deforms, Cauchy's first equation of motion reduces to

$$\nabla \cdot \boldsymbol{\sigma} = \boldsymbol{0}. \tag{2.11}$$

A neo-Hookean hyperelastic material model was employed to determine the Cauchy stress tensor. The constitutive model was selected and calibrated to experimental data through the procedure outlined in Section 2.2.2.

2.2.2 Calibration and selection of constitutive model

To reproduce the murine cranial dura mater's stress-strain behavior *in silico*, a hyperelastic material model was applied. Several uniaxial [20, 24, 26, 27] and biaxial [16, 19] loading studies—across multiple mammals (human, rat, and pig)—have shown that cranial dura mater deforms non-linearly, requiring that a hyperelastic constitutive model must be used to solve for the Cauchy stress. The models were calibrated to *ex vivo* stress-stretch data of rodent cranial dura mater under uniaxial

loading [20]. Because of the significant similarities between mouse and rat head anatomy [59, 60], the murine stress-strain curve was assumed to follow a similar profile to the rodent, thus the data from Maikos et al. [20] was used for model calibration.

Three potential models were investigated: the neo-Hookean (NH), Mooney-Rivlin (MR), and Ogden (O) model. The Cauchy stress of a hyperelastic material is dependent on a strain energy function, a scalar-valued function that relates the energy required to deform a material to the deformation gradient [63]. For an isotropic material, the strain energy functions, $\Psi(\lambda_1, \lambda_2, \lambda_3)$, with respect to the three principal stretches, follow:

$$\Psi_{\mathrm{NH}}(\lambda_1, \lambda_2, \lambda_3) = \mu(\lambda_1^2 + \lambda_2^2 + \lambda_3^2 - 3), \tag{2.12}$$

$$\Psi_{\mathrm{MR}}(\lambda_1, \lambda_2, \lambda_3) = C_1(\lambda_1^2 + \lambda_2^2 + \lambda_3^2 - 3) + C_2(\lambda_1^2\lambda_2^2 + \lambda_2^2\lambda_3^2 + \lambda_3^2\lambda_1^2 - 3), \tag{2.13}$$

$$\Psi_{\mathrm{O}}(\lambda_1, \lambda_2, \lambda_3) = \sum_{i=1}^{N} \frac{u_i}{\alpha_i}(\lambda_1^{\alpha_i} + \lambda_2^{\alpha_i} + \lambda_3^{\alpha_i} - 3). \tag{2.14}$$

The constants μ, C_1, C_2, and u_i are a measure of material rigidity or stiffness. Because this is an incompressible material, the accuracy of the model rests in the approximation of the stiffness. The three different models offer varying complexity. The neo-Hookean estimates the shear modulus, μ, directly, while the Ogden model can be tuned, to the N^{th} parameter. N= 3 is often more than sufficient to accurately replicate the non-linear stress-strain behavior of biological tissues [20].

The Cauchy stress for an incompressible hyperelastic material with respect to the principal stretches takes the form:

$$\boldsymbol{\sigma} = -p + \lambda_a \frac{\partial \Psi(\lambda_a)}{\partial \lambda_a}, \quad \text{where} \quad a = 1, 2, 3, \tag{2.15}$$

where p is an internal pressure that must be determined. Given the calibration data

comes from a uniaxial tension test and the material is considered incompressible, the principal stretches are dependent on a single scalar stretch value ($\lambda_1 = \lambda$, thus $\lambda_2 = \lambda_3 = \frac{1}{\sqrt{\lambda}}$). Additionally, because the dura samples' boundaries are free, aside from the connection to the tensile testing equipment, the Cauchy stresses in the normal directions are zero. This allows p to be computed, greatly simplifying the determination of the expression for Cauchy stress in the direction of loading:

$$\boldsymbol{\sigma}_{\mathrm{NH}}(\lambda) = 2\mu(\lambda - \frac{1}{\lambda^2}), \tag{2.16}$$

$$\boldsymbol{\sigma}_{\mathrm{MR}}(\lambda) = (2C_1 + \frac{2C_2}{\lambda})(\lambda^2 - \frac{1}{\lambda}), \tag{2.17}$$

$$\boldsymbol{\sigma}_{\mathrm{O}}(\lambda) = 2\sum_{i=1}^{N} u_i(\lambda^{\alpha_i} - \lambda^{-\frac{1}{2}\alpha_i}). \tag{2.18}$$

The nominal or engineering stress is obtained by dividing Equations 2.16, 2.17, and 2.18 by λ.

A curve-fitting algorithm calibrated the unknown parameters (μ, C_1, C_2, u_i, and α_i) of the constitutive models to nominal stress-stretch data from Maikos et al. [20]. The model parameters were fit only to the first half of the experimental data because we were primarily interested in the initial stretching ($0 - 10\%$ strain). The stress-stretch curve of each constitutive model against the calibration data (Figure 2.5) indicate the success of each model and their fitted parameters (Table 2.4), at recreating the material behavior.

Although the Ogden model (N=3) precisely recreates the rodent cranial dura mater stress-stretch curve, the neo-Hookean model was chosen for the *in silico* model. This choice was motivated by the nature of the current study. The present investigation is primarily interested in how improvements of model geometry influence the determined *in vivo* pre-stretch. Effects of curvature and asymmetry were placed at a higher priority than material characteristics, however, it was important that the tissue was modeled as a non-linear elastic material. Thus, neo-Hookean assump-

tions sufficiently capture that behavior, but avoid the mathematical complexity of the Ogden model (N=3).

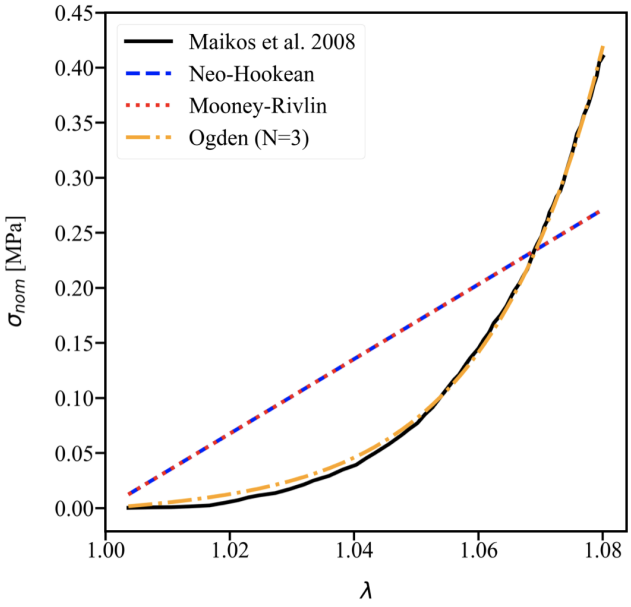

Figure 2.5. Curve fit of hyperelastic material models to stress-stretch curve of uniaxially loaded rat cranial dura, obtained from Maikos et al. [20]. The model's were calibrated within a stretch of 1.00 to 1.08, as the in-silico models primarily deform through this elastic region.

Ultimately, the murine cranial dura mater was modeled as a nearly incompressible, homogeneous, isotropic, neo-Hookean solid. To avoid numerical issues, the material was computationally modeled as "nearly" incompressible (Poisson's ratio > 0.45),

$$\Psi_{\mathrm{NH}}(\boldsymbol{C}^{\mathrm{e}}, J^{\mathrm{e}}) = \frac{\mu}{2}\left[\mathrm{tr}(\boldsymbol{C}^{\mathrm{e}}) - 3 - 2\ln\left(J^{\mathrm{e}}\right)\right] + \frac{L}{2}\ln^2\left(J^{\mathrm{e}}\right), \tag{2.19}$$

where $\boldsymbol{C}^{\mathrm{e}} = (\boldsymbol{F}^{\mathrm{e}})^T \cdot \boldsymbol{F}^{\mathrm{e}}$ is the elastic right Cauchy Green deformation tensor. This required the introduction of the second Lamé constant, L, which is related to the bulk

TABLE 2.4

COEFFICIENTS OF CALIBRATED HYPERELASTIC CONSTITUTIVE MODELS

Coefficient	Model	Value
μ (MPa)	Neo-hookean	1.13
C_1 (MPa)	Mooney-Rivlin	0.56
C_2 (MPa)	Mooney-Rivlin	2.76×10^{-10}
G_1 (MPa)	Ogden (N=3)	3.57×10^{-15}
α_1	Ogden (N=3)	2.76
G_2 (MPa)	Ogden (N=3)	4.92×10^{-3}
α_2	Ogden (N=3)	57.74
G_3 (MPa)	Ogden (N=3)	3.64×10^{-15}
α_3	Ogden (N=3)	3.16×10^{-3}

modulus and describes a material's response to uniform hydrostatic pressure, thus defining the compressibility. When computationally modeling nearly incompressible materials, an experimentally determined bulk modulus is not required, but rather L can be assumed to be significantly larger than the shear modulus ($\geq 1000\mu$).

The Cauchy stress with respect to $\boldsymbol{b}^{\mathrm{e}}$ and J^{e} is given by

$$\boldsymbol{\sigma} = \frac{1}{J^{\mathrm{e}}}[\mu \boldsymbol{b}^{\mathrm{e}} + (L \ln(J^{\mathrm{e}}) - \mu)\boldsymbol{I}], \tag{2.20}$$

with the elastic left Cauchy Green deformation tensor, $\boldsymbol{b}^{\mathrm{e}} = \boldsymbol{F}^{\mathrm{e}} \cdot (\boldsymbol{F}^{\mathrm{e}})^T$.

2.2.3 *In silico* model geometry and boundary conditions

The neonatal and adult dura mater were modeled as thin, three-dimensional 1/8 ellipsoids. The axes sizes, thickness, and initial cut lengths/locations were determined through further idealization of the skull dimensions (Table 2.2). The cranial dimensions were used as proxies for the dural dimensions because of the tissue's rigid conformity to the extremely thin bone, making for nearly negligible differences between the two tissues lengths, widths, and heights.

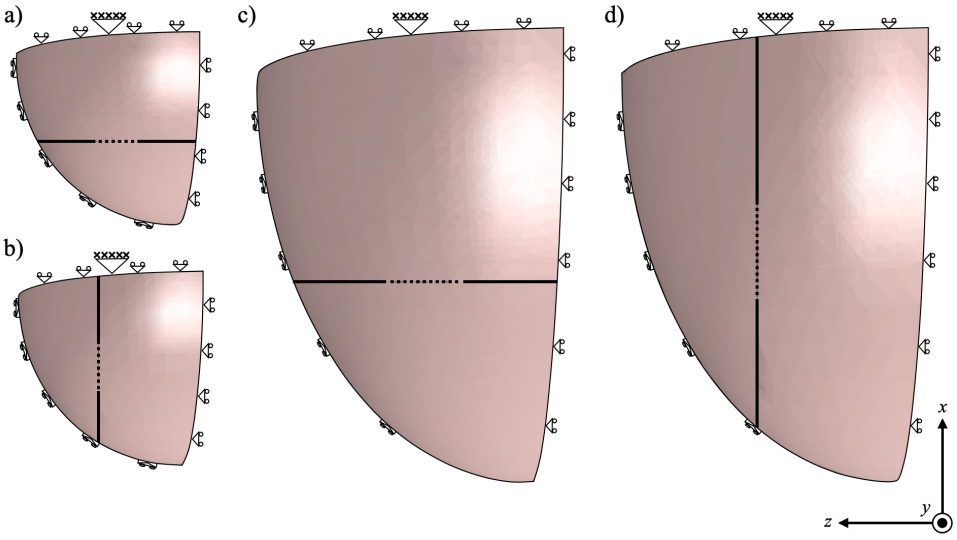

Figure 2.6. *In silico* models of neonatal, a) and b), and adult, c) and d), murine cranial dura mater. Symmetry along the anatomical reference planes (axial, coronal, and sagittal) were used to simplify the models into 1/8 ellipsoids. The axial plane is the x-z plane, the coronal plane is the y-z plane, and the sagittal plane is the x-y plane. Roller constraints were imposed perpendicular to faces lying on the axial, coronal, and sagittal planes. The deforming dura mater has a surface-to-surface interaction with a fixed rigid shell, ensuring there is no change in curvature throughout stretching. Models were partitioned into two parts along either the middle of the major, a) and c), or minor, b) and d), axis. The split parts were joined with tie constraints (solid black line), while the initial length of the dura incision was left unconstrained (dotted black line).

Starting as a full ellipsoid, symmetry along the anatomical reference planes (axial, coronal, and sagittal) were used to simplify the models into 1/8 ellipsoids. The axial plane is the x-z plane, the coronal plane is the y-z plane, and the sagittal plane is the x-y plane. Qualitatively, the neonatal and adult cranium have roughly a hemi-ellipsoidal shape when cut along the axial plane. The hemi-ellipsoid was reduced to a 1/4 ellipsoid by considering the dural cuts were exclusively performed in the parietal lobe. Existing experimental measurements of ICR mice cranial lobe lengths [64] reported that the parietal, interparietal, and occipital lobes made up roughly half (51.65%) of the total length (excluding the nasal lobe). With the actual percentage close to half of the total length, it was deemed appropriate to assume axisymmetric boundary conditions along the coronal plane of the hemi-ellipsoid. The new 1/4 ellipsoid model was 51.65% of ex-vivo length.

Finally, looking at the anterior and posterior views, it was observed that both the neonatal and adult mice skulls were fairly symmetric along the sagittal plane. Thus, the 1/4 ellipsoid was assumed symmetric along the sagittal plane, resulting in the final 1/8 ellipsoid. The 1/8 ellipsoid had a major axis (a) of 51.65% of the *ex vivo* measured length, and two equally sized minor axes (b and c) 50% of the *ex vivo* measured width. The width was chosen over the height for the minor axis size because the incisions occurred in the superior position over the axial plane. The axes sizes for the neonatal models are included in Table 2.5 with the model thickness determined in Section 2.1.2.

The simulation of the dural incisions were accomplished by splitting the 1/8 ellipsoid into two parts, leaving the center of the partition unconstrained. Experimentally, Dr. Oberman performed *ex vivo* incisions from the superior position, with intention to cut in the middle of the medial-lateral distance of the parietal dura. This process was emulated in the computational model, in which the 1/8 ellipsoid was partitioned along the axial plane in 1) the middle of the major axis for the transverse incision

and 2) the middle of the minor axis for the longitudinal incision. The two parts were then tied together above and below the cuts. Tie constraints enforce that there is no relative motion between connected nodes, even if nodes are not directly aligned along the boundary. The initial length of the transverse, a_t, and longitudinal, a_l, cuts (included in Table 2.5), or the unconstrained regions, were the average length of the measured *ex vivo* incisions determined in Section 2.1.2.

TABLE 2.5

IN SILICO MODEL DIMENSIONS, THICKNESS, AND INITIAL CUT LENGTHS

Age group	a (mm)	b (mm)	c (mm)	t (mm)	a_t (mm)	a_l (mm)
Neonate	4.480	4.278	4.278	0.00081	1.058	1.823
Adult	9.622	6.506	6.506	0.00138	1.753	2.557

Two models were created with different boundary conditions: neonatal ICR mouse dura mater with transverse (Figure 2.6a) and longitudinal (Figure 2.6b) cuts, and adult with transverse (Figure 2.6c) and longitudinal (Figure 2.6d) cuts. Each deformable domain was subjected to a surface-to-surface interaction with a rigid shelled part to maintain the geometry's curvature throughout deformation. The rigid shell had identical axis sizes to the dura mater's axes with the thickness subtracted. The rigid part was fixed at a reference point, restricting any translation of the deformable body. Roller conditions were assigned along all exposed faces of the dural model, with motion in the y-direction constrained along the axial plane, x-direction constrained

along the coronal plane, and z-direction constrained along the sagittal plane.

The deformable domains were discretized with four-noded linear tetrahedra, hybrid elements with linear pressure variation (C3D4H). This element type was selected as it offered improved convergence for non-linear geometries. The transverse isotropic in-plane stretching was applied at the integration point of each element. For all models, the integration point was a single Gaussian point inside the element. Linear triangular (R3D3) and quadrilateral (R3D4) rigid elements were used for the contact interactions. The total number of elements for each simulation, organized by element type, have been listed in Table 2.6.

TABLE 2.6

TOTAL NUMBER OF ELEMENTS WITHIN EACH *IN SILICO* MODEL

Age group	Cut orientation	C3D4H	R3D3	R3D3
Neonate	Transverse	88054	204	7397
Neonate	Longitudinal	77239	204	7397
Adult	Transverse	219458	768	22903
Adult	Longitudinal	260503	768	22903

2.2.4 Numerical simulation and convergence criterion

The constitutive model was implemented in Abaqus/Standard by modifying an existing user-defined material (UMAT) subroutine [65]. A UMAT was necessary to apply the material and mathematical model since the full analysis cannot be constructed with Abaqus's built-in options.

Convergence was improved by changing the solution correction criterion. Initial convergence issues were product of the near-incompressibility assumption; the model underwent rigid body deformation with practically no change in volume, known to Abaqus as "zero volume flux" [66]. When zero volume flux occurs, convergence requires the residual of the volume field, r^V_{max}, of the current Newton iteration, to be less than the magnitude of the volume flux, $\tilde{q}^V$, multiplied by the criterion for zero flux, ϵ^α,

$$r^V_{max} \leq \epsilon^\alpha \tilde{q}^V. \tag{2.21}$$

If this inequality is satisfied, the iteration converges if the largest correction to the volume field's solution, C^V_{max}, is less than a scalar multiple of the largest change in volume between increments, Δu^V_{max},

$$C^V_{max} \leq C^\alpha_\epsilon \Delta u^V_{max}. \tag{2.22}$$

In finite element analyses, correction is required to retain solution continuity across the discretized domain [67]. Convergence issues arise within zero volume flux cases when Equation 2.21 is satisfied, but Equation 2.22 is not. Such is the case of the current simulations, as the "nearly" incompressible assumption allows the volume to occasionally change between integration points, requiring larger solution corrections. When this happens, C^V_{max} can be larger than the change in volume between the current and previous increments, Δu^V_{max}. Thus, the iteration does not converge because Equation 2.22 is not satisfied, even if the residual of the volume field is much lower than $\epsilon^\alpha \tilde{q}^V$. To improve convergence, C^α_ϵ was increased from 0.001 to 0.01, to allow the simulation to converge with marginally higher solution corrections, while the allowable residual was not increased [66]. Otherwise, the default convergence criterion for implicit iteration within Abaqus/Standard was used.

CHAPTER 3

RESULTS AND DISCUSSION

3.1 Results

In silico models of pre-stretched neonatal and adult murine cranial dura mater with transverse and longitudinal incisions were created and numerically simulated in Abaqus/Standard. Comparison of the *in silico* and *ex vivo* incision opening dimensions allowed for the determination of the *in vivo* in-plane pre-stretch of the experimentally tested tissue.

The average opening width over length ratios for each age group and cut orientation were computed for the experimental samples ($v_{ex\ vivo}/a_{ex\ vivo}$) and numerical simulations ($v_{in\ silico}/a_{in\ silico}$). Incision opening ratios allowed the cut dimensions to be compared independent of initial cut length. $v_{ex\ vivo}/a_{ex\ vivo}$ for the neonate transverse and longitudinal cuts were 0.169 ± 0.048 and 0.100 ± 0.042, respectively (Table 3.1). $v_{ex\ vivo}/a_{ex\ vivo}$ for the adult transverse and longitudinal cuts were 0.237 ± 0.067 and 0.093 ± 0.0413, respectively (Table 3.1). The mean experimental incision opening ratios (Figure 3.1, dotted black line) were plotted atop the change in *in silico* incision opening ratios as in-plane stretch, λ, increases (Figure 3.1, solid black line).

Unlike Henderson et al. [28], we determined *in vivo* pre-stretch in the plane transverse to the surface's undeformed unit normal vector, rather than directional stretches. The "in-plane" pre-stretch is equibiaxial and does not inform of differences between stretch along the planar principal axes. However, the magnitude differences of the in-plane pre-stretch between the cut orientations indicate whether the anterior-posterior or medial-lateral directions were differently strained. The opening

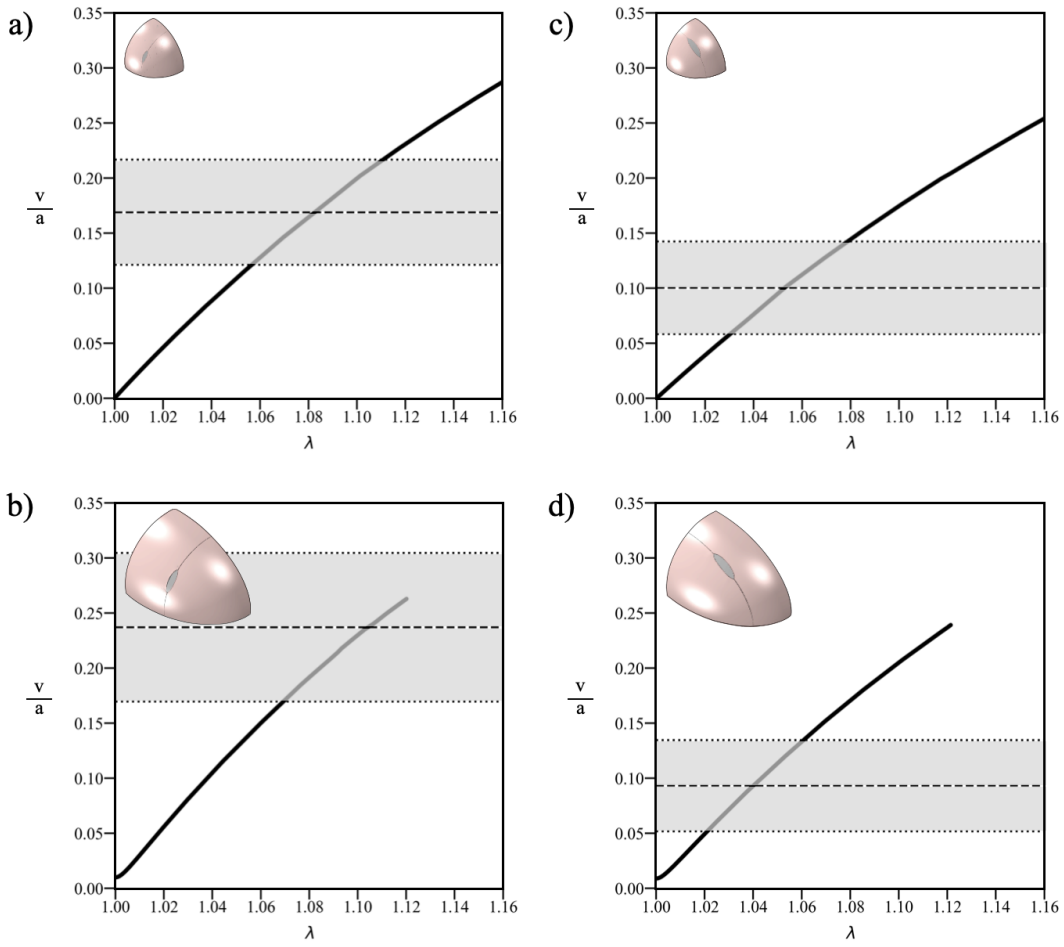

Figure 3.1. $v_{in\ silico}/a_{in\ silico}$ was plotted against the prescribed in-plane pre-stretch (λ) for the simulation of transverse (a and b) and longitudinal (c and d) dural incisions. $v_{ex\ vivo}/a_{ex\ vivo}$ was plotted (dotted black line) atop the curves, with the standard deviation of these measurements shadowed in grey. In comparing a) and b), the adult experienced significantly higher *in vivo* in-plane pre-stretch, while c) and d) show the neonate experienced slightly higher stretching.

width:length ratio for neonatal transverse dural incision (Figure 3.1a) was associated with an average in-plane pre-stretch of 1.083, while incision opening for the adult transverse dural incision (Figure 3.1b) corresponded to an average in-plane pre-stretch of 1.104. Both the experimental incision opening ratios for neonate and adult longitudinal incisions were markedly lower, with corresponding average in-plane pre-stretches of 1.053 (Figure 3.1c) and 1.040 (Figure 3.1d), respectively. Higher

recorded in-plane stretches were associated with the transverse incisions, suggesting larger anterior-posterior stretching. Smaller deformation post-longitudinal cut imply less significant medial-lateral strain. Unequal stretching supports the conclusion that *in vivo* murine cranial dura mater behaves anisotropically and/or experiences anisotropic residual strain.

The standard deviation of the samples (grey-shaded region) were plotted atop the computational curves to highlight the potentially large variation in experimental pre-stretch. The minimum, $\lambda_{\min}$, and maximum, $\lambda_{\max}$, *in vivo* in-plane pre-stretches corresponding with the *ex vivo* incision opening ratios' standard deviations were determined via linear interpolation. While the adult transverse incision's simulated data did not capture the maximum *ex vivo* incision opening ratio, extrapolation via fitting a fifth-order polynomial offered an estimation for the adult transverse cut's maximum stretch. The determined *in vivo* in-plane pre-stretches for the *ex vivo* dural incision experiment have been detailed in Table 3.1, with the corresponding age-group and *ex vivo* incision opening width-length ratios.

3.2 Discussion

3.2.1 Numerical simulation of pre-stretched murine cranial dura mater

The first objective of this study was to create a robust *in silico* model of *in vivo* pre-stretched murine cranial dura mater. The presented model sought to improve upon Henderson et al. [28], by better capturing the *in situ* tissue size, geometry and curvature. The previous model considered the dura mater as a two-dimensional rectangle, while the current model is a three-dimensional 1/8 ellipsoid. The main advantage of modeling the dura mater as an ellipsoid is the ability to include the effects of asymmetric curvature on incision opening. This improvement made the *in silico* incision openings more suitable comparisons to the *ex vivo* incision openings.

A three-dimensional computational model was designed to emulate *in situ* tissue

TABLE 3.1

DETERMINED *IN VIVO* DURAL PRE-STRETCH AND *EX VIVO* INCISION OPENING RATIOS

Age group	Cut orientation	$v_{ex\ vivo}/a_{ex\ vivo}$	λ_{ave}	λ_{min}	λ_{max}
Neonate	Transverse	0.169 ± 0.048	1.083	1.057	1.111
Neonate	Longitudinal	0.100 ± 0.042	1.053	1.030	1.079
Adult	Transverse	0.237 ± 0.067	1.104	1.069	1.143
Adult	Longitudinal	0.093 ± 0.041	1.040	1.021	1.061

curvature because the incisions were relatively large compared to the skull/dura's width and length, causing the curvature to vary along the incision. The average transverse cut lengths were 12.37% and 13.47% of the parietal lobe widths for the neonate and adult, respectively. The average longitudinal cut lengths for the newborn and adult were 21.02% and 13.73% of the frontal-parietal lengths, respectively. The incisions cover an appreciable amount of the sample's length and width, to the extent that they curved with the cranium. The 1/8 ellipsoid with experimentally measured axes allowed for the effects of the asymmetric curvature of the *in situ* environment to be considered.

Conversely, the two-dimensional model used by Henderson et al. [28] does not account for any geometric affects. Henderson et al. [28] argues that their plane stress model is appropriate because the incisions were small relative to the curvature of the dura. However, comparison of the incision opening length to skull/dura dimensions invalidate this assumption. Henderson et al. [28] created 4.04 ± 0.79mm transverse and 5.31 ± 0.98mm longitudinal incisions in adult Sprague-Dawley rats. *In vivo* measurements of adult Sprague-Dawley rat skulls reported a total parietal lobe width

of 17.11mm and mean frontal-parietal length of 24.54mm. Here, skull dimensions were obtained by averaging across the "soft diet" and "hard diet" groups from Abed et al. [68]. Consequentially, the previous study's transverse cuts would be on average 23.61% of the parietal lobe width, while their longitudinal cuts were 21.64% of the frontal-parietal length. Akin to the current study, their incision lengths are relatively too large to ignore the effects of curvature on tissue retraction, affirming the necessity of the presented model. Neglecting these effects likely leads to greater over-estimation of dura pre-stretch, especially if using linear elasticity because of the direct relationship between applied strains and incision opening dimensions.

3.2.2 Determination of *in vivo* pre-stretch

The second objective was to determine the *in vivo* pre-stretch of the experimental tissue. Isotropic in-plane pre-stretches were successfully estimated for both age-groups and incision orientations (Table 3.1). Differences in stretch across the cut orientations offer information about directional differences in the pre-stretch. Increased in-plane pre-stretch determined for the *ex vivo* transverse incision opening ratios indicate there is significantly larger anterior-posterior or longitudinal stretching than medial-lateral or transverse stretching. Additional qualitative comparison clearly shows the transverse cuts deform noticeably more in both the adult and neonatal cranial dura (Figures A.1, A.2, A.3, and A.4). Henderson et al. [28] quantitatively corroborates this finding by reporting statistically significantly larger average longitudinal residual strains ($6.11 \pm 3.62\%$) than average transverse residual strains ($3.82 \pm 2.64\%$).

Higher reported longitudinal pre-stretch is interesting in light of the prior finding [28], suggesting the dura mater of small mammals (mice and rats) may also be materially anisotropic. However, this conclusion contradicts other studies which showed the cranial dura mater of larger mammals is globally isotropic [20, 21, 26, 32, 62]. The apparent mechanical anisotropy of both rodent and murine cranial dura mater might

imply that the mechanical behavior is species-dependent. Scanning electron microscopic imagery [21, 26, 32] and small angle light scattering of human cranial dura [62] indicate that the tissue lacks any global fiber uniformity, essentially being a collection of highly uniform patches. Similar fiber alignment was found in smaller mammals via Polarized light microscopy imaging of rat cranial dura [20]. However, comparison of cranial rat dura from [28] to human dura quantitatively show rodent dura mater has noticeably longer and frequent longitudinal fibers, with small and less-frequent transverse fibers. Variation across mammals is common for biological tissues, and has even been proven for lumbar dura when comparing rodents, canines, and humans [20, 32]. Microscopic imaging may provide further evidence of this phenomena in murine cranial dura.

The averaged magnitude of the determined *in vivo* in-plane pre-stretch offer additional physiological implications of the dural pre-stretch. We found an average (across the two cut orientations) in-plane pre-stretch of 1.068 and 1.072 in neonatal and adult mice, respectively. This would imply that the dura is likely less compliant *in vivo*. The stress-stretch curve for the *ex vivo* testing of rodent cranial dura (Figure 2.5) highlight the exponential change in stiffness. The dura mater physically changes between stiffness regimes; the tissue's collagen fibrils are wavy and loose when softer, and successively uncrimp as the material stiffens. With average in-plane residual strains of 6.8% and 7.2%, the dura mater's collagen fibers are expected to be fairly taut. This is advantageous for limiting further deformation which could damage the tissue vasculature or extracellular matrix. Increased rigidity may also serve to restrain motion of the brain. For example, the dura mater that separates the cerebral hemispheres (the falx cerebri) is significantly more rigid than the surrounding tissue and laterally constrains brain deformation [69]. Finally, we postulate that reductions in dural pre-stretch may increase the likelihood of premature cranial suture fusion. Fong et al. [13] found that important cytokines for neurocranial remodeling (TGF-

β1 and FGF-2) were up-regulated under increased mechanical strain in dura cells. If dural pre-stretch was reduced, the *in vivo* tissue would experience greater stretching, prematurely triggering protein expression and ossification of the cranial sutures. Future investigations of pre-stretch in pathological cranial dura mater may provide support this hypothesis.

3.2.3 Age-dependency of murine cranial dura mater pre-stretch

The final objective was to examine the age-dependency of the *in vivo* in-plane pre-stretch. The neonatal and adult pre-stretch were compared, with the hopes of elucidating how the elastic deformation of the tissue changed throughout growth, and the implications this might have on cranial suture fusion. Although the small sample size poorly represents the mouse population, the quantitative and qualitative results suggest age-dependent characteristics of murine cranial dura.

We found similar pre-stretches in both directions of the neonatal mouse, suggesting that immature dura might be more isotropic, or at least stretched more isotropically, than the adult. Qualitatively, when looking at the neonatal cranium (Figure 2.2, left), the parietal, interparietal, and occipital lobes appear to create a relatively spherical shape, as opposed to the adult's hemi-elliptic shape. While geometry might not play into the material anisotropy, bipedal mammals with more rounded heads (humans) have isotropic dura [21, 26, 32, 62].

However, neonatal mice dura behaving isotropically directly contradicts Henderson et al. [28], who found significantly higher longitudinal residual strain in immature rats and overall larger average residual strains among younger age groups. They remark that increased longitudinal strain is plausible because the cranial vault is set to grow more longitudinally rather than transversely. Their findings are corroborated by *in vitro* examinations of immature rodent dura cell mechanosensitivity [13, 14]. Greenwald et al. [14] demonstrated that newborn rat cells (day six) were significantly more biologically active than adult cells (day 60), and Fong et al. [13] calculated a

maximum equibiaxial strain of 9.7% in neonatal (day zero) rodent cells, as opposed to 0.1% in adult (day 60) rodent cells. One potential reason for the current study's inconsistent findings may be tracked to differences in neonatal and adult mice skull stiffness.

Like Henderson et al. [28], particular care was taken to leave the *ex vivo* dura firmly attached to the calvaria, to capture *in situ* conditions. However, the neonatal cranium is so thin, small, and thus highly deformable, that the immature cranium likely deformed during the dural incision. Potential evidence of the soft skull's impact may come from reviewing the relaxation of the dura across the two age-groups. Relaxation of the dura mater was quantitatively examined by computing the percent difference in incision opening lengths and widths (at half of the length) between $t = 0$ min and $t = 5$ min. First, the percent differences (e_a and e_v) were computed for all a and v measurements in Table A.1,

$$e_a = 100 \times \frac{a_{t=0} - a_{t=5}}{a_{t=0}} \quad \text{and} \quad e_v = 100 \times \frac{v_{t=0} - v_{t=5}}{v_{t=0}}. \tag{3.1}$$

Then, all e_a and e_v were averaged to get δ_a and δ_v, respectively. A small δ_a (< 1.5) for both age-groups and cut orientations indicate there was virtually no incision length change over time (Table 3.2). Conversely, δ_v for the adult transverse incisions was much larger than the neonate's (Table 3.2). One could posit that the relatively small changes in neonatal transverse cut dimensions after relaxation are due to the immature skull deforming with the dura, thus releasing more strain energy. This could potentially explain why pre-stretch associated with the transverse incisions was lower for the neonatal tissue. However, δ_v for the longitudinal incisions do not wholly support this hypothesis; the neonatal average percent difference in incision opening length was greater than the adults (10.956% versus 5.166%) (Table 3.2). Alternatively, these results may say more about the directional dependency of the

murine cranial dura, rather than the age dependency.

TABLE 3.2

ABSOLUTE AVERAGE PERCENT DIFFERENCE BETWEEN INCISION OPENING LENGTH (a) AND WIDTH (v) AT $t = 0$ MIN AND $t = 5$ MIN

Age-group	Cut orientation	δ_a (%)	δ_v (%)
Neonate	Transverse	0.014	0.135
Neonate	Longitudinal	0.724	10.956
Adult	Transverse	1.359	7.464
Adult	Longitudinal	1.416	5.166

The differences in cranial softness and incision relaxation has not been previously discussed by Henderson et al. [28], indicating that this might not impact the dural pre-stretch of larger Muridae. Unfortunately, scarcity of test subjects make conclusions about the influence of cranial softness and geometry on age-dependent pre-stretch more hypotheses than theories. Furthermore, although the current study provides some evidence of age-dependent pre-stretch, conclusions about the mechanosensitivity of the dura and its role in cranial suture fusion will require additional experimentation. The value of the current investigation rests in providing a new, more robust *in silico* model and mathematical framework for numerical simulation of cranial dura pre-stretch.

3.3 Limitations

3.3.1 Experimental limitations

The investigation is heavily limited by a small experimental size ($n = 5$ neonate, $n = 6$ adult). This impacted the estimation of the cranial, and thus the dural, measurements for length, height, and width. With more samples, averaged dimensions better representative of the average newborn and mature ICR mice could have been determined and applied to the *in silico* model. More importantly, the lacking sample size bring into question the validity of the magnitude of the determined *in vivo* pre-stretch. For example, the in-plane pre-stretch associated with the neonatal transverse dural incisions was estimated based on the incision opening ratios from just two subjects. These incision opening ratios significantly differed (range = ± 0.048), making $\lambda_{\max}$ and $\lambda_{\min}$ drastically different than λ_{ave}. The neonatal longitudinal and both adult incisions also saw similar standard deviations. Incision opening measurements from more subjects may not change λ_{ave}, but give us an idea of the true variability among individuals.

The measurements of the skull and incision lengths and widths were impacted by the inherent limitations of ImageJ. Firstly, measurements made using ImageJ were visually approximated. Secondly, the precision of the measurements was restricted by the resolution of the images. Precision was dependent on the image scale, with 4x magnification being fairly precise, yet still not fine enough to measure the thickness of the mouse skull and dura across both age groups, requiring estimation from previous experimental data [58, 61]. This ties into the third limitation, in that relative error of distance measurements increased as magnitude of the dimension decreased [28]. For larger measurements, such as the cranium dimensions, mismeasuring by a few pixels has significantly less of an impact on the accuracy of the measurement, as opposed to the incision widths or lengths. By this logic, the neonatal incision opening dimensions

had a larger error than the adult for images of the same magnification.

Increasing the magnification helped minimize measurement error, yet, it could not overcome implicit limitations of image-based measurement. Firstly, all measurements were the euclidean distance between points. This was done so that the experiment may be more easily reproduced, however, this method fails to capture any slight curving of the cut length or width. Secondly, image quality influenced the accurate determination of incised tissue's retraction boundaries. This was a case-by-case hindrance, as some images (Figure A.2, V) the open cut is fairly clear, while the boundaries in others (Figure A.4, V) were extremely difficult to ascertain.

Like imageJ, the cutting method has fundamental drawbacks. The cutting method discounts small stretching that results from the thickness of the scalpel blade (Figure 3.2). Roughly 0.4mm thick [70], the no. 11 blade scalpel would create an incision up to 0.4mm wide. As represented by Figure 3.2, the dural tissue could have been pushed apart by the scalpel, rather than retracted following the release of residual stress. Any incisions openings less than or equal to this width may have been associated with over-estimations of pre-stretch. Secondly, the cutting method primarily approximates stretch perpendicular to the cut; the width of the opening is the only real indication of residual strain.

The cutting method also only approximates residual strain in its local environment. However, an argument can be made that the tissue and cut's relative scale determines the weight of this limitation. As stated in Section 3.2.1, the incisions made within the immature and mature dura were relatively large, with average incision opening lengths between 12.37% and 21.02% of the total dimension along which they were cut. Pairing the small, thin, non-linear geometry of the murine cranial dura mater with the average incision lengths, one can posit that the global behavior is captured and that this is likely a greater limitation for larger tissues. Conversely, the test subject's small size increased the difficulty of preforming the cuts.

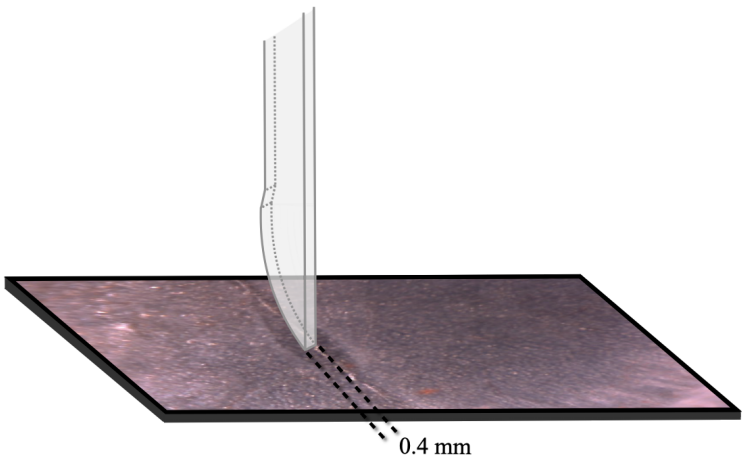

Figure 3.2. Representation of the scalpel blade separating the dura mater, rather than tissue retracting following the release of residual stress. Artificially opened incisions due to the 0.4mm thick [70] blade may lead to over-estimations of *in vivo* pre-stretch.

Dr. Oberman attempted to make all incisions along the middle of medial-lateral distance within the parietal lobe. In practice this was quite difficult because the samples were free to move throughout cutting, for constraining them could potentially damage the dura. Yet, the act of cutting posed a greater threat to tissue damage, and lead to the significant reduction in usable dural incision measurements. Early on, the incisions were performed with a no. 15 blade scalpel, which unfortunately tore through the neonatal cranium and damaged a few adult skulls. Switching to no. 11 blades improved the quality of the cuts; however, quite a few immature dura samples were torn in other locations prior to imaging. In these cases, mutilation could have occurred prior to incision during dissection. Similar issues were not mentioned in the prior work, even though Henderson et al. [28] used no. 15 blades, indicating this may be a greater issue for smaller muridae. Finally, the overall slitting experiment must be considered an estimation of *in vivo* pre-stretch because cutting was performed *ex vivo*. The mechanical behavior of hydrated, *in situ* tissue may be more reminiscent of *in vivo* dura, but does not directly recreate the strain response of living cells.

3.3.2 Computational limitations

The fidelity of the numerical simulations was hindered by necessary assumptions about dura mater material properties, *in situ* geometry, and mathematical model of pre-stretch. Despite improving significantly upon previous *in silico* models [28], the lack of mouse calibration data, simplicity of the neo-Hookean model, geometric idealization, and numerical simulation of transverse isotropic stretching, limited the exactness of the current simulations.

The neonatal and adult constitutive models were calibrated to the same mature rodent cranial dura stress-stretch data. While the dura mater of the two species may have similar stress-strain profiles, the actual stiffness is likely different because of the different scales. Similarly, size and age differences suggest the stiffness of newborn cranial dura mater is different than mature dura. Qualitatively, this is assumed because of the immature tissue's decreased vasculature. Quantitatively, differences in estimated *in vivo* in-plane pre-stretch between the examined age-groups indicate that other mechanical properties—like stiffness—must be age-dependent. Thereby, the implied stiffness from the fitted shear and estimated bulk modulus must be slightly more off for the neonate than adult model. The absence of prior experimental characterization of the material behavior of murine cranial dura left no reasonable alternatives other than assuming the same model parameters for the neonatal tissue. Fortunately, this limitation was less consequential because capturing the non-linear deformation of the dura mater was more important than using exact material constants.

The neo-Hookean constitutive model described the non-linear elasticity of the mouse dura mater, but failed to approximate change in stiffness as stress increased. As evidenced by the calibration study (Table 2.4), the shear modulus (μ), and thus the Cauchy stress of an isotropic, nearly incompressible, neo-Hookean solid, is defined by a single fitted parameter. Moreover, this material parameter was only calibrated

to the soft regime ($\lambda = 1$ to 1.08), meaning the rapid increase in stiffness from $\lambda = 1.08$ to 1.16, was ignored. Higher order hyperelastic models, such as the Ogden (N=3) model, used more material dependent coefficients to very accurately emulate the entire deformation of a tissue (Figure 2.5). Prior studies [20, 23] corroborate that Ogden (N=3) is the ideal constitutive model for other mammalian cranial dura mater. Other higher order alternatives—the Skalak, Tozeren, Zarda and Chien model—also closely replicate the non-linear deformation of human dura mater [16, 19]. The neo-Hookean model was accepted because the current analysis was more focused on the effects of curvature and geometric asymmetries, however, future *in silico* works should treat murine dura as an Ogden (N=3) solid. Subsequent investigations may also want to incorporate anisotropic pre-stretch and material viscoelasticity. As the results indicate, murine dural pre-stretch is likely directional dependent, yet, the current model only applied uniform stretching. Computational models of human dura need not consider material directionality because of the overwhelming evidence of fiber isotropy [5, 21, 26, 32, 62]. However, all future simulations of mammalian cranial dura mater should have time-coupled deformation. Human [22], rodent [20, 28, 29], and now mouse dura mater (Table A.1), has been recorded relaxing following loading and incising.

Increased geometric complexity came with numerous subsidiary limitations. Firstly, equal semi-axes of the 1/8 ellipsoid do not account for the *ex vivo* measured height of the neonatal and adult dura mater. This changes the curvature of the ellipsoid, potentially skewing the incision opening dimensions. Secondly, the models had homogeneous thickness. Most biological tissues have varying thickness—and mouse dura mater should not be expected to be an exception. Previous studies have reported that human dura mater varies in thickness throughout the calvaria [30, 31]. However, because of how thin mammalian dura mater is, especially murine dura, heterogeneous thickness may have a nearly negligible impact on mechanical behavior. Thus, it was

more important to ballpark the average thickness, which again had to be estimated because there are no experimental measurements of neonatal or adult murine cranial dura mater thickness. Thirdly, the effects of imperfections are inherently lost when simplifying the mouse dura mater into an ellipsoid. Alternatives to the finite element method, such as isogeometric analysis, offer the opportunity to capture convolutions and defects *in vivo* tissue structure [71].

Finally, the mathematical model and numerical simulation of transverse isotropic stretching raised particular limitations. The *in silico* model experienced isotropic pre-stretch, yet, differences between the longitudinal and transverse *ex vivo* incision opening ratios clearly show murine dura mater is anisotropically pre-stretched. Application of anisotropic pre-stretch would likely lead to differently sized incision opening dimensions at different amounts of residual strain. For these reasons, the determined *in vivo* in-plane pre-stretch provides valuable insight into pre-stretch directionality and age-dependency, but less reliably describes the actual magnitude of the pre-stretch.

Convergence issues occurred when numerically solving the mathematical framework within Abaqus/Standard. Although the convergence parameter, C_{ϵ}^{α}, was changed to address convergence issues that were product of the near incompressibility assumption (Section 2.2.4), the adult simulations failed to converge to the final prescribed in-plane pre-stretch of 1.16. This required λ_{max} for the adult transverse cut orientation to be extrapolated after preforming a polynomial fit of the *in silico* model's incision opening ratio-stretch curve.

CHAPTER 4

CONCLUSIONS

4.1 Summary

Two accurately sized *in silico* models of neonatal and adult murine cranial dura mater with longitudinal or transverse incisions were created (Figure 2.6). The dura mater was modeled as a homogeneous, isotropic, hyperelastic solid. A neo-Hookean constitutive model was calibrated to experimental data of rat dura mater under uniaxial loading, as this offered the closest approximation of the murine dura mater stress-strain relationship. The constitutive model was implemented in Abaqus/Standard using a UMAT subroutine. The calibrated *in silico* models were numerically simulated under isotropic in-plane stretching transverse to the domain's undeformed surface normal. Comparison of the *in silico* and *ex vivo* incision opening ratios allowed for the determination of the *in vivo* in-plane pre-stretch associated with the *ex vivo* incision openings. Significantly larger in-plane pre-stretch for both the neonatal and adult transverse cuts indicate cranial dura mater pre-stretch is anisotropic. This finding is consistent with studies of previously sized mammals [20, 28]. Qualitative review of the incision opening images further support anisotropic material behavior (Figures A.1, A.2, A.3, A.4). The results suggest murine cranial dura mater pre-stretch is age-dependent; the immature dura appears potentially more isotropic and experiences less anterior-posterior (longitudinal) residual strain. A small sample size (n=5 neonate, n=6 adult) limit the reliability of conclusions about age-dependency. Regardless, ancillary characterization of material behavior, such as the anisotropy of murine dural pre-stretch, highlight the importance of capturing the asymmetry and

non-linearity of biological tissues with *in silico* models. Determining *in vivo* mechanical properties of biological tissue provide insight into how common pathologies may arise; in the case of the cranial dura mater, elucidating the tissue's role in cranial suture fusion.

4.2 Future directions

The discussion of the experimental (Section 3.3.1) and computational (Section 3.3.2) limitations suggest several reasonable improvements for subsequent investigations. Experimentally, the reliability of the determined *in vivo* in-plane pre-stretch would be greatly improved with an increased sample size. Henderson et al. [28] recorded measurements for 41 mice, nearly four times the amount used in this study. Supplying additional *ex vivo* neonatal transverse incisions would alone improve confidence of the directionality and age-dependency conclusions. Mathematically, the neo-Hookean hyperelastic model should be replaced with the Ogden (N=3). Higher order constitutive models are proven to optimally emulate the mechanical behavior of mammalian dura mater [16, 19, 20, 23]. Geometrically, the *in silico* model should be changed from an $a > b = c$ ellipsoid, to an $a > b \neq c$ ellipsoid. This would alter the curvature of the current model, accounting for the experimentally measured height of the cranium/dura samples. More lofty improvements would include the application of anisotropic pre-stretching and an automated algorithm for cut boundary identification. Simulation of directionally dependent pre-stretch would require the development of a new mathematical model—one compatible with the Ogden (N=3) formulation of the constitutive equations. Finally, creation of a imaging processing pipeline compatible with ImageJ could improve the fidelity of incision opening boundary measurements, minimizing human error.

APPENDIX A

SUPPLEMENTARY FIGURES AND TABLES

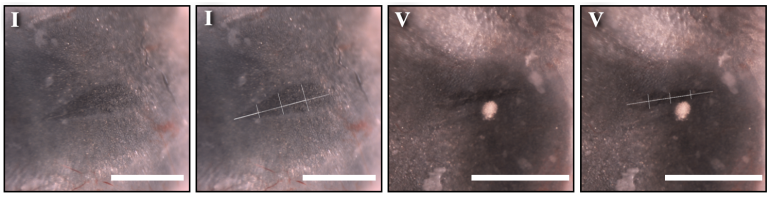

Figure A.1. Processed images of neonatal murine cranial dura mater with transverse incisions at $t = 5\,\text{min}$. Subjects I and V were imaged at 3x and 4x magnification, respectively. The original images were paired with their annotated counterparts. All scale bars indicate 1 mm.

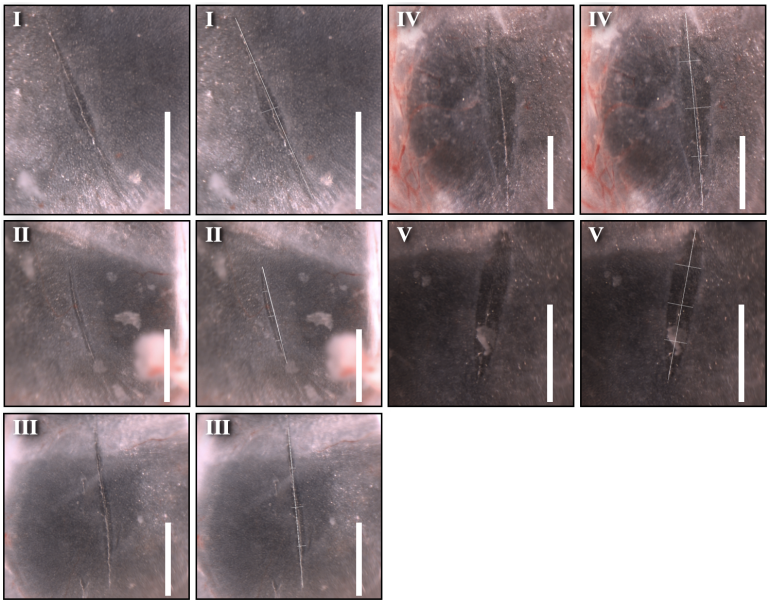

Figure A.2. Processed images of neonatal murine cranial dura mater with longitudinal incisions at $t = 5\,\text{min}$. Subjects I and V were imaged at 4x magnification. Subjects II, III, and IV were imaged at 3x magnification. The original images were paired with their annotated counterparts. All scale bars indicate 1 mm.

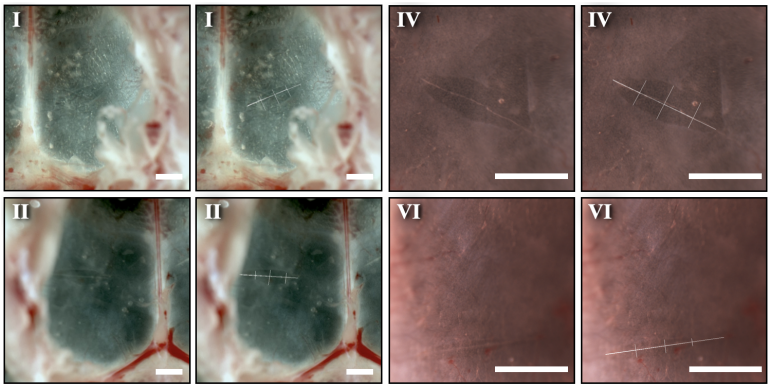

Figure A.3. Processed images of adult murine cranial dura mater with transverse incisions at $t = 5\,\text{min}$. Subjects I and II were imaged at 1x magnification. Subjects IV and VI were imaged at 3x magnification. The original images were paired with their annotated counterparts. All scale bars indicate 1 mm.

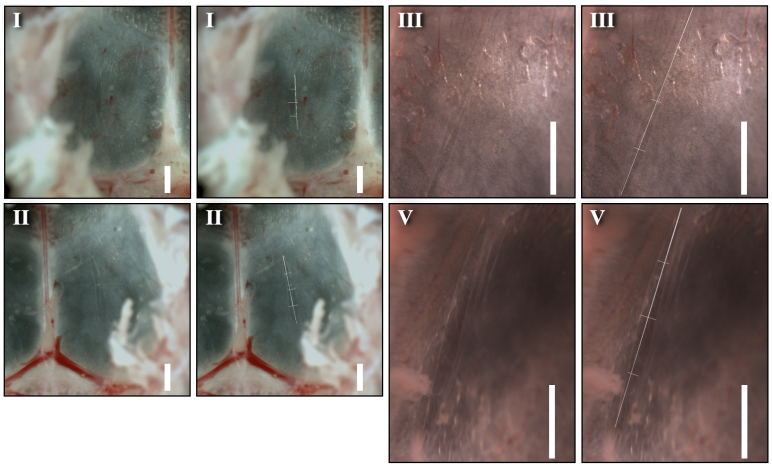

Figure A.4. Processed images of adult murine cranial dura mater with longitudinal incisions at $t = 5\,\text{min}$. Subjects I and II were imaged at 1x magnification. Subjects III and V were imaged at 3x magnification. The original images were paired with their annotated counterparts. All scale bars indicate 1 mm.

TABLE A.1:

EX VIVO DURAL INCISION WIDTH AND LENGTH MEASUREMENTS AT $t = 0\,\text{MIN}$ AND $t = 5\,\text{MIN}$

			$t = 0\,\text{min}$				$t = 5\,\text{min}$			
Age-group	Subject	Cut orientation	a	$v(0.25a)$	$v(0.50a)$	$v(0.75a)$	a	$v(0.25a)$	$v(0.50a)$	$v(0.75a)$
Neonate	I	transverse	1.266	0.147	0.246	0.270	1.237	0.174	0.276	0.351
Neonate	V	transverse	0.867	0.123	0.121	0.087	0.086	0.146	0.103	0.086
Neonate	I	longitudinal	1.875	0.062	0.140	0.061	1.860	0.073	0.168	0.069
Neonate	II	longitudinal	1.251	0.057	0.071	0.060	1.245	0.067	0.079	0.071
Neonate	III	longitudinal	2.026	0.081	0.127	0.092	2.030	0.077	0.142	0.111
Neonate	IV	longitudinal	2.468	0.247	0.320	0.239	2.441	0.276	0.331	0.213
Neonate	V	longitudinal	1.526	0.243	0.233	0.207	1.510	0.265	0.254	0.225
Adult	I	transverse	2.090	0.510	0.554	0.416	2.067	0.585	0.557	0.464
Adult	II	transverse	2.142	0.242	0.399	0.365	2.128	0.322	0.498	0.435
Adult	IV	transverse	1.508	0.368	0.475	0.348	1.480	0.370	0.475	0.351
Adult	VI	transverse	1.316	0.183	0.204	0.124	1.293	0.186	0.195	0.136
Adult	I	longitudinal	2.192	0.222	0.332	0.249	2.1353	0.217	0.314	0.249
Adult	II	longitudinal	2.586	0.194	0.265	0.262	2.521	0.226	0.279	0.308
Adult	III	longitudinal	2.571	0.082	0.122	0.137	2.572	0.079	0.130	0.144
Adult	V	longitudinal	2.950	0.147	0.196	0.169	2.933	0.145	0.203	0.136

* Measurements reported in millimeters.

* When possible, both cut orientations were performed for a single subject.

BIBLIOGRAPHY

1. Jing Jin, Sahar Shahbazi, John Lloyd, Sidney Fels, Sandrine De Ribaupierre, and Roy Eagleson. Hybrid simulation of brain–skull growth. *SIMULATION*, 90 (1):3–10. ISSN 0037-5497. doi: 10/f56d3x. URL https://doi.org/10.1177/0037549713516691. Publisher: SAGE Publications Ltd STM.

2. Joseph Libby, Arsalan Marghoub, David Johnson, Roman H. Khonsari, Michael J. Fagan, and Mehran Moazen. Modelling human skull growth: a validated computational model. *Journal of The Royal Society Interface*, 14(130): 20170202. doi: 10/gk9j6v. URL https://royalsocietypublishing.org/doi/full/10.1098/rsif.2017.0202.

3. Johannes Weickenmeier, Cedric Fischer, Dennis Carter, Ellen Kuhl, and Alain Goriely. Dimensional, geometrical, and physical constraints in skull growth. *Physical Review Letters*, 118(24):248101. doi: 10/gbkxkw. URL https://link.aps.org/doi/10.1103/PhysRevLett.118.248101.

4. James H Henderson, Michael T Longaker, and Dennis R Carter. Sutural bone deposition rate and strain magnitude during cranial development. *Bone*, 34(2):271–280, . ISSN 8756-3282. doi: 10/b8mnht. URL https://www.sciencedirect.com/science/article/pii/S8756328203003983.

5. Marina Protasoni, Simone Sangiorgi, Andrea Cividini, Gloria Tiffany Culuvaris, Giustino Tomei, Carlo Dell'Orbo, Mario Raspanti, Sergio Balbi, and Marcella Reguzzoni. The collagenic architecture of human dura mater: Laboratory investigation. *Journal of Neurosurgery*, 114(6):1723–1730. ISSN 0022-3085, 1933-0693. doi: 10.3171/2010.12.JNS101732. URL https://thejns.org/view/journals/j-neurosurg/114/6/article-p1723.xml.

6. Joan T. Richtsmeier and Kevin Flaherty. Hand in glove: brain and skull in development and dysmorphogenesis. *Acta Neuropathologica*, 125:469–489. doi: https://doi-org.proxy.library.nd.edu/10.1007/s00401-013-1104-y.

7. Gloria Fabris, Zeynep M. Suar, and Mehmet Kurt. Micromechanical heterogeneity of the rat pia-arachnoid complex. *Acta Biomaterialia*, 100:29–37. ISSN 17427061. doi: 10.1016/j.actbio.2019.09.044. URL https://linkinghub.elsevier.com/retrieve/pii/S1742706119306658.

8. Jeffrey R. Gagan, Sunil S. Tholpady, and Roy C. Ogle. Cellular dynamics and tissue interactions of the dura mater during head development. *Birth Defects Research Part C: Embryo Today: Reviews*, 81(4):297–304. ISSN 1542-9768. doi: 10.1002/bdrc.20104. URL http://onlinelibrary.wiley.com/doi/abs/10.1002/bdrc.20104.

9. Carolyn Renzulli Jaslow. Mechanical properties of cranial sutures. *Journal of Biomechanics*, 23(4):313–321. ISSN 0021-9290. doi: 10/b2c4p8. URL https://www.sciencedirect.com/science/article/pii/002192909090059C.

10. J.J. Mao. Mechanobiology of craniofacial sutures. *Journal of Dental Research*, 81(12):810–816. ISSN 0022-0345. doi: 10/cb2jtw. URL https://doi.org/10.1177/154405910208101203.

11. Roy C. Ogle, Sunil S. Tholpady, Kathryn A. McGlynn, and Rebecca A. Ogle. Regulation of cranial suture morphogenesis. *Cells, Tissues, Organs*, 176(1):54–66. ISSN 1422-6405. doi: 10/d5kjqm.

12. Jill Peterson and Paul C. Dechow. Material properties of the human cranial vault and zygoma. *The Anatomical Record Part A: Discoveries in Molecular, Cellular, and Evolutionary Biology*, 274A(1):785–797. ISSN 1552-4892. doi: 10.1002/ar.a.10096. URL http://onlinelibrary.wiley.com/doi/abs/10.1002/ar.a.10096.

13. Kenton D. Fong, Stephen M. Warren, Elizabeth G. Loboa, James H. Henderson, Tony D. Fang, Catherine M. Cowan, Dennis R. Carter, and Michael T. Longaker. Mechanical strain affects dura mater biological processes: Implications for immature calvarial healing:. *Plastic and Reconstructive Surgery*, 112(5):1312–1327. ISSN 0032-1052. doi: 10.1097/01.PRS.0000079860.14734.D6. URL http://journals.lww.com/00006534-200310000-00014.

14. Joshua A. Greenwald, Babak J. Mehrara, Jason A. Spector, Stephen M. Warren, Francesca E. Crisera, Peter J. Fagenholz, Pierre J. Bouletreau, and Michael T. Longaker. Regional differentiation of cranial suture-associated dura mater in vivo and in vitro: Implications for suture fusion and patency. *Journal of Bone and Mineral Research*, 15(12):2413–2430. ISSN 1523-4681. doi: 10.1359/jbmr.2000.15.12.2413. URL https://onlinelibrary.wiley.com/doi/abs/10.1359/jbmr.2000.15.12.2413.

15. Hasan Emre Aydın, Ceren Kızmazoglu, Ismail Kaya, Bugra Husemoglu, Gulden Sozer, Hasan Havıtcıoglu, and Ali Arslantas. Biomechanical properties of the cranial dura mater with puncture defects : An in vitro study. *Journal of Korean Neurosurgical Society*, 62(4):382–388. ISSN 2005-3711. doi: 10.3340/jkns.2018.0130. URL https://www.ncbi.nlm.nih.gov/pmc/articles/PMC6616988/.

16. Donita I. Bylski, Timothy J. Kriewall, Nuri Akkas, and John W. Melvin. Mechanical behavior of fetal dura mater under large deformation biaxial tension. *Journal of Biomechanics*, 19(1):19–26. ISSN 0021-9290. doi: 10.

1016/0021-9290(86)90105-3. URL https://www.sciencedirect.com/science/article/pii/0021929086901053.

17. Dries De Kegel, Julie Vastmans, Heleen Fehervary, Bart Depreitere, Jos Vander Sloten, and Nele Famaey. Biomechanical characterization of human dura mater. *Journal of the Mechanical Behavior of Biomedical Materials*, 79:122–134. ISSN 17516161. doi: 10.1016/j.jmbbm.2017.12.023. URL https://linkinghub.elsevier.com/retrieve/pii/S1751616117305684.

18. Amit Gefen, Nurit Gefen, Qiliang Zhu, Ramesh Raghupathi, and Susan S. Margulies. Age-dependent changes in material properties of the brain and braincase of the rat. *Journal of Neurotrauma*, 20(11):1163–1177. ISSN 0897-7151, 1557-9042. doi: 10.1089/089771503770802853. URL http://www.liebertpub.com/doi/10.1089/089771503770802853.

19. T. J. Kriewall, N. Akkas, D. I. Bylski, J. W. Melvin, and B. A. Work. Mechanical behavior of fetal dura mater under large axisymmetric inflation. *Journal of Biomechanical Engineering*, 105(1): 71–76. ISSN 0148-0731, 1528-8951. doi: 10.1115/1.3138388. URL https://asmedigitalcollection.asme.org/biomechanical/article/105/1/71/398291/Mechanical-Behavior-of-Fetal-Dura-Mater-Under.

20. Jason T. Maikos, Ragi A.I. Elias, and David I. Shreiber. Mechanical properties of dura mater from the rat brain and spinal cord. *Journal of Neurotrauma*, 25(1):38–51. ISSN 0897-7151, 1557-9042. doi: 10.1089/neu.2007.0348. URL http://www.liebertpub.com/doi/10.1089/neu.2007.0348.

21. Kathleen A. McGarvey, J. Michael Lee, and Derek R. Boughner. Mechanical suitability of glycerol-preserved human dura mater for construction of prosthetic cardiac valves. *Biomaterials*, 5(2):109–117. ISSN 0142-9612. doi: 10.1016/0142-9612(84)90011-5. URL https://www.sciencedirect.com/science/article/pii/0142961284900115.

22. J. W. Melvin, J. H. McElhaney, and V. L. Roberts. Development of a mechanical model of the human head — determination of tissue properties and synthetic substitute materials. *SAE Transactions*, 79:2685–2694. ISSN 0096-736X. URL http://www.jstor.org/stable/44723768. Publisher: SAE International.

23. Baptiste Pierrat, Louise Carroll, Florence Merle, David B. MacManus, Robert Gaul, Caitríona Lally, Michael D. Gilchrist, and Aisling Ní Annaidh. Mechanical characterization and modeling of the porcine cerebral meninges. *Frontiers in Bioengineering and Biotechnology*, 8:801. ISSN 2296-4185. doi: 10.3389/fbioe.2020.00801. URL https://www.frontiersin.org/article/10.3389/fbioe.2020.00801/full.

24. R. van Noort, M. M. Black, T. R. P. Martin, and S. Meanley. A study of the uniaxial mechanical properties of human dura mater preserved in glycerol. *Bio-*

materials, 2(1):41–45. ISSN 0142-9612. doi: 10.1016/0142-9612(81)90086-7. URL https://www.sciencedirect.com/science/article/pii/0142961281900867.

25. F Vandenabeele, J Creemers, and I Lambrichts. Ultrastructure of the human spinal arachnoid mater and dura mater. *Journal of Anatomy*, 189:417–430. ISSN 0021-8782. URL https://www.ncbi.nlm.nih.gov/pmc/articles/PMC1167758/.

26. Lloyd Wolfinbarger Jr., Yongxing Zhang, Bao-Ling T. Adam, Diana Homsi, Kevin Gates, and Vicki Sutherland. Biomechanical aspects on rehydrated freeze-dried human allograft dura mater tissues. *Journal of Applied Biomaterials*, 5(3):265–270. ISSN 1549-9316. doi: 10.1002/jab.770050313. URL http://onlinelibrary.wiley.com/doi/abs/10.1002/jab.770050313.

27. Johann Zwirner, Mario Scholze, John Neil Waddell, Benjamin Ondruschka, and Niels Hammer. Mechanical properties of human dura mater in tension – an analysis at an age range of 2 to 94 years. *Scientific Reports*, 9(1):16655. ISSN 2045-2322. doi: 10.1038/s41598-019-52836-9. URL http://www.nature.com/articles/s41598-019-52836-9.

28. James H Henderson, Randall P Nacamuli, Betty Zhao, Michael T Longaker, and Dennis R Carter. Age-dependent residual tensile strains are present in the dura mater of rats. *Journal of The Royal Society Interface*, 2(3):159–167, . ISSN 1742-5689, 1742-5662. doi: 10.1098/rsif.2005.0035. URL https://royalsocietypublishing.org/doi/10.1098/rsif.2005.0035.

29. Alexander V. Shulyakov, Stefan S. Cenkowski, Richard J. Buist, and Marc R. Del Bigio. Age-dependence of intracranial viscoelastic properties in living rats. *Journal of the Mechanical Behavior of Biomedical Materials*, 4(3):484–497. ISSN 17516161. doi: 10.1016/j.jmbbm.2010.12.012. URL https://linkinghub.elsevier.com/retrieve/pii/S1751616110001876.

30. Maged D. Fam, Andrea Potash, Martin Potash, Robert Robinson, Lucy Karnell, Erin O'Brien, and Jeremy D. W. Greenlee. Skull base dural thickness and relationship to demographic features: A postmortem study and literature review. *Journal of Neurological Surgery. Part B, Skull Base*, 79(6):614–620. ISSN 2193-6331. doi: 10.1055/s-0038-1651501. URL https://www.ncbi.nlm.nih.gov/pmc/articles/PMC6239876/.

31. H Kuchiwaki, S Inao, N Ishii, Y Ogura, and S P Gu. Human dural thickness measured by ultrasonographic method: reflection of intracranial pressure. *Journal of Ultrasound in Medicine*, 16(11):725–730. ISSN 1550-9613. doi: 10.7863/jum.1997.16.11.725. URL http://onlinelibrary.wiley.com/doi/abs/10.7863/jum.1997.16.11.725.

32. Dennis J. Patin, Eugene C. Eckstein, Kirk Harum, and Vicente S. Pallares. Anatomic and biomechanical properties of human lumbar

dura mater. *Anesthesia & Analgesia*, 76(3):535–540. ISSN 0003-2999. URL https://journals.lww.com/anesthesia-analgesia/Abstract/1993/03000/Anatomic_and_Biomechanical_Properties_of_Human.14.aspx.

33. H.C. Han and Y.C. Fung. Residual strains in porcine and canine trachea. *Journal of Biomechanics*, 24(5):307–315, . ISSN 00219290. doi: 10.1016/0021-9290(91)90349-R. URL https://linkinghub.elsevier.com/retrieve/pii/002192909190349R.

34. H. C. Han and Y. C. Fung. Direct measurement of transverse residual strains in aorta. *American Journal of Physiology-Heart and Circulatory Physiology*, 270 (2):H750–H759, . ISSN 0363-6135, 1522-1539. doi: 10.1152/ajpheart.1996.270.2.H750. URL https://www.physiology.org/doi/10.1152/ajpheart.1996.270.2.H750.

35. Manuel K. Rausch and Ellen Kuhl. On the effect of prestrain and residual stress in thin biological membranes. *Journal of the Mechanics and Physics of Solids*, 61(9):1955–1969. ISSN 00225096. doi: 10.1016/j.jmps.2013.04.005. URL https://linkinghub.elsevier.com/retrieve/pii/S0022509613000768.

36. Ramesh N. Vaishnav and Jafar Vossoughi. Residual stress and strain in aortic segments. *Journal of Biomechanics*, 20(3):235–239. ISSN 00219290. doi: 10.1016/0021-9290(87)90290-9. URL https://linkinghub.elsevier.com/retrieve/pii/0021929087902909.

37. Seckin Aydin, Baris Kucukyuruk, Bashar Abuzayed, Sabri Aydin, and Galip Zihni Sanus. Cranioplasty: Review of materials and techniques. *Journal of Neurosciences in Rural Practice*, 02(2):162–167. ISSN 0976-3147, 0976-3155. doi: 10.4103/0976-3147.83584. URL http://www.thieme-connect.de/DOI/DOI?10.4103/0976-3147.83584.

38. Alessandro Borghi, Naiara Rodriguez-Florez, Will Rodgers, Gregory James, Richard Hayward, David Dunaway, Owase Jeelani, and Silvia Schievano. Spring assisted cranioplasty: A patient specific computational model. *Medical Engineering & Physics*, 53:58–65. ISSN 1350-4533. doi: 10/gddzmw. URL https://www.sciencedirect.com/science/article/pii/S1350453318300079.

39. Bashar Abuzayed, Ali Metin Kafadar, Şöhret Ali Oğuzoğlu, Bülent Canbaz, and Mehmet Yasar Kaynar. Duraplasty using autologous fascia lata reenforced by on-site pedicled muscle flap: Technical note. *Journal of Craniofacial Surgery*, 20(2):435–438. ISSN 1049-2275. doi: 10.1097/SCS.0b013e31819b968f. URL https://journals.lww.com/00001665-200903000-00035.

40. Jack Y. Ghannam and Khalid A. Al Kharazi. *Neuroanatomy, Cranial Meninges*. StatPearls Publishing. URL https://www.ncbi.nlm.nih.gov/books/NBK539882/.

41. Victor Kekere and Khalid Alsayouri. *Anatomy, Head and Neck, Dura Mater*. StatPearls Publishing. URL https://www.ncbi.nlm.nih.gov/books/NBK545301/. Publication Title: StatPearls [Internet].

42. Dae Chul Suh. Where did the dura mater come from? *Neurointervention*, 15(1):2–3. ISSN 2093-9043. doi: 10.5469/neuroint.2020.00045. URL https://www.ncbi.nlm.nih.gov/pmc/articles/PMC7105093/.

43. Susan W. Herring. Mechanical influences on suture development and patency. *Frontiers of oral biology*, 12:41–56. ISSN 1420-2433. doi: 10.1159/0000115031. URL https://www.ncbi.nlm.nih.gov/pmc/articles/PMC2826139/.

44. Jack C. Yu, Steven R. Buchman, Arun K. Gosain, Robert J. Havlik, Tien-Hsiang Wang, Po-Sang Lam, and Mohamad Masoumy. Basic biomechanics for craniofacial surgeons: The responses of alloplastic materials and living tissues to mechanical forces. *FACE*, 2(4):446–461. ISSN 2732-5016. doi: 10/gnxx3x. URL https://doi.org/10.1177/27325016211060232.

45. Y C Fung and S Q Liu. Change of residual strains in arteries due to hypertrophy caused by aortic constriction. *Circulation research*, 65(5):1340–1349, 1989. ISSN 0009-7330.

46. Alexey V. Kamenskiy, Iraklis I. Pipinos, Yuris A. Dzenis, Carol S. Lomneth, Syed A. Jaffar Kazmi, Nicholas Y. Phillips, and Jason N. MacTaggart. Passive biaxial mechanical properties and in vivo axial pre-stretch of the diseased human femoropopliteal and tibial arteries. *Acta Biomaterialia*, 10(3):1301–1313, . ISSN 17427061. doi: 10.1016/j.actbio.2013.12.027. URL https://linkinghub.elsevier.com/retrieve/pii/S1742706113006296.

47. Alexey V. Kamenskiy, Iraklis I. Pipinos, Yuris A. Dzenis, Nicholas Y. Phillips, Anastasia S. Desyatova, Justin Kitson, Robert Bowen, and Jason N. MacTaggart. Effects of age on the physiological and mechanical characteristics of human femoropopliteal arteries. *Acta Biomaterialia*, 11:304–313, . ISSN 17427061. doi: 10.1016/j.actbio.2014.09.050. URL https://linkinghub.elsevier.com/retrieve/pii/S1742706114004425.

48. H. Gregersen, G.S. Kassab, and Y.C. Fung. REVIEW: The zero-stress state of the gastrointestinal tract:. *Digestive Diseases and Sciences*, 45(12):2271–2281. ISSN 1573-2568. doi: 10.1023/A:1005649520386. URL https://doi.org/10.1023/A:1005649520386.

49. Adrián Buganza Tepole, Michael Gart, Chad A. Purnell, Arun K. Gosain, and Ellen Kuhl. Multi-view stereo analysis reveals anisotropy of prestrain, deformation, and growth in living skin. *Biomechanics and modeling in mechanobiology*, 14(5):1007–1019, . ISSN 1617-7959. doi: 10.1007/s10237-015-0650-8. URL https://www.ncbi.nlm.nih.gov/pmc/articles/PMC4520804/.

50. H. R. Chaudhry, B. Bukiet, T. Findley, and A. B. Ritter. Evaluation of residual stress in rabbit skin and the relevant material constants. *Journal of Theoretical Biology*, 192(2):191–195. ISSN 00225193. doi: 10.1006/jtbi.1997.0616. URL https://linkinghub.elsevier.com/retrieve/pii/S0022519397906160.

51. Adrián Buganza Tepole, Michael Gart, Arun K. Gosain, and Ellen Kuhl. Characterization of living skin using multi-view stereo and isogeometric analysis. *Acta Biomaterialia*, 10(11):4822–4831, . ISSN 17427061. doi: 10.1016/j.actbio.2014.06.037. URL https://linkinghub.elsevier.com/retrieve/pii/S1742706114002931.

52. Gang Xu, Philip V. Bayly, and Larry A. Taber. Residual stress in the adult mouse brain. *Biomechanics and modeling in mechanobiology*, 8(4):253–262. ISSN 1617-7959. doi: 10.1007/s10237-008-0131-4. URL https://www.ncbi.nlm.nih.gov/pmc/articles/PMC4605564/.

53. Wolfgang Bothe, Manuel K. Rausch, John-Peder Escobar Kvitting, Dominique K. Echtner, Mario Walther, Neil B. Ingels, Ellen Kuhl, and D. Craig Miller. How do annuloplasty rings affect mitral annular strains in the normal beating ovine heart? *Circulation*, 126(11). ISSN 0009-7322, 1524-4539. doi: 10.1161/CIRCULATIONAHA.111.084046. URL https://www.ahajournals.org/doi/10.1161/CIRCULATIONAHA.111.084046.

54. Manuel K. Rausch, Wolfgang Bothe, John-Peder Escobar Kvitting, Serdar Göktepe, D. Craig Miller, and Ellen Kuhl. In vivo dynamic strains of the ovine anterior mitral valve leaflet. *Journal of Biomechanics*, 44(6):1149–1157. ISSN 00219290. doi: 10.1016/j.jbiomech.2011.01.020. URL https://linkinghub.elsevier.com/retrieve/pii/S0021929011000509.

55. Andrew A. Sharp, Alicia M. Ortega, Diego Restrepo, Douglas Curran-Everett, and Ken Gall. In vivo penetration mechanics and mechanical properties of mouse brain tissue at micrometer scales. *IEEE Transactions on Biomedical Engineering*, 56(1):45–53. ISSN 1558-2531. doi: 10.1109/TBME.2008.2003261.

56. Edward K. Rodriguez, Anne Hoger, and Andrew D. McCulloch. Stress-dependent finite growth in soft elastic tissues. *Journal of Biomechanics*, 27(4):455–467. ISSN 0021-9290. doi: 10.1016/0021-9290(94)90021-3. URL http://www.sciencedirect.com/science/article/pii/0021929094900213.

57. W. S. Rasband. Imagej. URL https://imagej.nih.gov/ij/.

58. Ahmet Kinaci, Wilhelmina Bergmann, Ronald LAW Bleys, Albert van der Zwan, and Tristan PC van Doormaal. Histologic comparison of the dura mater among species. *Comparative Medicine*, 70(2):170–175. ISSN 1532-0820. doi: 10.30802/AALAS-CM-19-000022. URL https://www.ncbi.nlm.nih.gov/pmc/articles/PMC7137549/.

59. G. M. Constantinescu. *Comparative anatomy of the mouse and the rat: a color atlas and text.* CRC Press, Taylor Francis Group., 2018. ISBN 9781138624030.

60. Jennifer Frohlich. Rats and mice. *Ferrets, Rabbits, and Rodents*, pages 345–367. doi: 10.1016/B978-0-323-48435-0.00025-3. URL https://www.ncbi.nlm.nih.gov/pmc/articles/PMC7258799/.

61. Meaghan A. O'Reilly, Aidan Muller, and Kullervo Hynynen. Ultrasound insertion loss of rat parietal bone appears to be proportional to animal mass at sub-megahertz frequencies. *Ultrasound in medicine & biology*, 37(11):1930–1937. ISSN 0301-5629. doi: 10.1016/j.ultrasmedbio.2011.08.001. URL https://www.ncbi.nlm.nih.gov/pmc/articles/PMC3228246/.

62. M. C. Jimenez Hamann, M. S. Sacks, and T. I. Malinin. Quantification of the collagen fibre architecture of human cranial dura mater. *Journal of Anatomy*, 192:99–106. ISSN 0021-8782. doi: 10.1046/j.1469-7580.1998.19210099.x. URL https://www.ncbi.nlm.nih.gov/pmc/articles/PMC1467743/.

63. Gerhard A. Holzapfel. *Non-linear solid mechanics: A Continuum Approach for Engineering*. Wiley. ISBN 978-0-471-82319-3.

64. Minoru Kawakami and Ken-ichi Yamamura. Cranial bone morphometric study among mouse strains. *BMC Evolutionary Biology*, 8(1):73. ISSN 1471-2148. doi: 10.1186/1471-2148-8-73. URL http://bmcevolbiol.biomedcentral.com/articles/10.1186/1471-2148-8-73.

65. Maria A. Holland. Hitchhiker's guide to abaqus. URL https://zenodo.org/record/1243270.

66. Michael Smith. *ABAQUS/Standard User's Manual, Version 6.14*. Dassault Systèmes Simulia Corp, United States, 2014.

67. Gaylen A. Thurston, John E. Reissner, Peter A. Stein, and Norman F. Knight. Error analysis and correction of discrete solutions from finite-element codes. *AIAA Journal*, 26(4):446–453. ISSN 0001-1452, 1533-385X. doi: 10.2514/3.9914. URL https://arc.aiaa.org/doi/10.2514/3.9914.

68. George S. Abed, Peter H. Buschang, Reginald Taylor, and Robert J. Hinton. Maturational and functional related differences in rat craniofacial growth. *Archives of Oral Biology*, 52(11):1018–1025. ISSN 00039969. doi: 10.1016/j.archoralbio.2007.05.008. URL https://linkinghub.elsevier.com/retrieve/pii/S0003996907001410.

69. D R S Bradshaw, J Ivarsson, C L Morfey, and D C Viano. Simulation of acute subdural hematoma and diffuse axonal injury in coronal head impact. *Journal of Biomechanics*, 34(1):85–94. doi: https://doi.org/10.1016/s0021-9290(00)00135-4.

70. Scalpel blade no. 11, Apr 2021. URL https://www.martor.com/en/products/blades/product/scalpel-blade-no-11.

71. Devin W. Laurence, Colton J. Ross, Ming-Chen Hsu, Arshid Mir, Harold M. Burkhart, Gerhard A. Holzapfel, and Chung-Hao Lee. Benchtop characterization of the tricuspid valve leaflet pre-strains. *Acta Biomaterialia*, page S1742706122005220. ISSN 17427061. doi: 10.1016/j.actbio.2022.08.046. URL https://linkinghub.elsevier.com/retrieve/pii/S1742706122005220.